

# Dynamics of Quantum Chiral Solitons

Leandro M. Chinellato

*Department of Physics and Astronomy, University of Tennessee, Knoxville, TN 37996, USA*

Oleg A. Starykh

*Department of Physics and Astronomy, University of Utah, Salt Lake City, UT 84112, USA*

Cristian D. Batista

*Department of Physics and Astronomy, University of Tennessee, Knoxville, TN 37996, USA and Neutron Scattering Division, Oak Ridge National Laboratory, Oak Ridge, Tennessee 37831, USA*

(Dated: December 10, 2025)

We introduce a non-perturbative framework for quantizing chiral solitons in interacting quantum spin chains. This approach provides a direct lattice extension of the well-established  $S$ -duality between the sine-Gordon and Thirring models, thereby bridging the gap between continuum dualities and their lattice counterparts. By constructing the quantum chiral-soliton operators explicitly, we show how their unconventional dynamics appear in the excitation spectrum and correlation functions across the full Brillouin zone. A key result is that the dominant soliton tunneling amplitude alternates in sign,  $\text{sgn}(t_{1+}) = (-1)^{2S+1}$ , sharply distinguishing half-odd-integer from integer spin chains. We further identify characteristic signatures of these chiral excitations in the dynamical spin structure factor, demonstrating their visibility in inelastic neutron scattering. Our results open a route to experimentally probing non-perturbative features of dual quantum field theories in condensed-matter settings.

## I. INTRODUCTION

The study of solitons has a long and rich history, beginning with the observations of solitary water waves propagating along narrow channels while maintaining their shape and without noticeable decay in the 19th century [1, 2]. These observations led to the derivation of the first nonlinear wave equation, the Korteweg - de Vries (KdV) equation, by the end of the century [3, 4].

The modern era of soliton physics began in the 1960s with the numerical demonstration that solitary wave solutions of the KdV equation behave as particle-like excitations that survive collisions essentially unchanged [5]. This behavior inspired the term *soliton*, now broadly used to refer to localized, non-singular solutions of nonlinear field equations that propagate without distortion and recover their original shape and velocity after interaction [6]. Solitons were subsequently identified in diverse physical contexts, including plasmas [7], nuclear physics through the Skyrme model of the nucleon [8–10], and condensed matter systems [11, 12].

Among the paradigmatic examples, the sine-Gordon model stands out for its mathematical elegance and broad physical relevance. This model is exactly integrable and supports both topological soliton and breather solutions, and has found applications ranging from dislocations in crystals to flux dynamics in Josephson junctions. Moreover, the celebrated  $S$ -duality between the sine-Gordon and massive Thirring models [13, 14] reveals a deep connection between bosonic and fermionic theories: sine-Gordon solitons map to Thirring fermions, while breathers correspond to fermion-antifermion bound states. This duality exemplifies how solitons can encode non-perturbative physics in

a dual, weakly coupled description.

Frustrated magnets provide an especially fertile ground for exploring soliton physics in quantum materials [15–23]. Their tunable interactions enable both accurate theoretical modeling and direct experimental detection of soliton-like excitations, for instance through inelastic neutron scattering. While solitons originate as classical objects, quantum fluctuations can substantially modify their properties.

In this work, we extend the  $S$ -duality to the lattice by deriving a model for weakly interacting fermions from the original spin model. This is done by directly “quantizing” the classical chiral sine-Gordon solitons that emerge in a  $D = 1 + 1$  frustrated spin chain. The approach begins with the construction of localized soliton creation and annihilation operators. Quantum fluctuations are systematically included through a Wannierization procedure, yielding a set of orthonormal quantum states that faithfully represent a “quantum soliton”. This formalism captures the quantum tunneling processes that endow solitons with mobility, resulting in a well-defined and non-trivial dispersion relation. In particular, the dominant soliton tunneling amplitude alternates in sign,  $\text{sgn}(t_{1+}) = (-1)^{2S+1}$ , sharply distinguishing half-odd-integer from integer spin chains. The soliton dynamics is described by an effective weakly coupled tight-binding fermionic Hamiltonian, whose band structure and dynamical properties are benchmarked against numerical simulations based on Density Matrix Renormalization Group (DMRG) and Matrix Product State (MPS) methods, showing excellent agreement.

In the classical limit of the theory, the soliton modes condense as the uniform magnetic field  $H$  is decreased below the saturation value  $H_c$ , while conventional magnon

excitations remain gapped. The softening of these classical chiral solitons drives the well-known commensurate–incommensurate (C–IC) phase transition into the incommensurate soliton lattice phase [17]. In the quantum version of the model, the duality shows that the softening of the fermionic mode associated with the quantum chiral soliton leads to a free-fermion fixed point, arising from the emergent U(1) symmetry associated with the conservation of topological charge. This free-fermion fixed point, confirmed by our DMRG simulations, marks the onset of a Tomonaga–Luttinger liquid phase—the quantum-mechanical counterpart of the classical IC soliton lattice phase.

Our results have different attractive aspects that are discussed at length in the conclusion section. First, they enable a “first principles” derivation of the effective fermionic model from the original spin model without the need of taking the continuum limit of both theories. This is important because it is not always possible to connect the parameters for the effective field theory with those of the original “high-energy theory”. The second attractive aspect is that lattice fermionic theory can be used to study the soliton dynamics over the full Brillouin zone, enabling the detection and characterization of the quantum chiral solutions via inelastic neutron scattering experiments. More generally, the procedure that we introduce here for quantizing classical solitons on the lattice can be generalized to solitons of other homotopy groups, such as Skyrmions [ $\Pi_3(SO(3)) \cong \mathbb{Z}$ ] and baby skyrmions [ $\Pi_2(S^2) \cong \mathbb{Z}$ ].

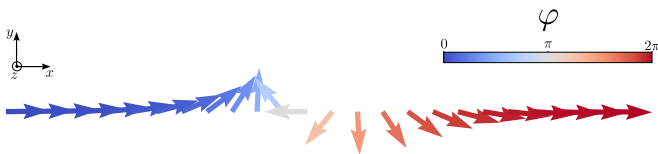


FIG. 1. Profile of the classical chiral soliton. Arrow directions indicate spin orientation, while their color encodes the value of the angle  $\varphi$ .

## II. MODEL AND CLASSICAL LIMIT

Although the sine–Gordon model admits multiple physical realizations across different areas of condensed matter and field theory, here we focus on a microscopic spin model whose continuum limit is described by the sine–Gordon field theory. Specifically, we consider a one-dimensional spin- $\frac{1}{2}$  ferromagnetic Heisenberg chain of length  $L$ , oriented along the  $x$ -axis and subject to a Dzyaloshinskii–Moriya (DM) interaction characterized by a vector  $\mathbf{D} = D\hat{z}$ . An external magnetic field  $\mathbf{H} = H\hat{x}$  is applied perpendicular to the DM vector. The Hamil-

tonian of the system is

$$\hat{H}_S = -\sum_{j=1}^L \left[ J \hat{\mathbf{S}}_j \cdot \hat{\mathbf{S}}_{j+1} + D(\hat{S}_j^x \hat{S}_{j+1}^y - \hat{S}_j^y \hat{S}_{j+1}^x) + H \hat{S}_j^x \right], \quad (1)$$

where  $J > 0$  and  $H = g\mu_B B$ , with  $\mu_B$  the Bohr magneton and  $g$  the gyromagnetic factor. It is important to note that the magnetic field is applied *transverse* to the  $U(1)$ -invariant axis set by the DM interaction. Consequently, the full Hamiltonian has only discrete symmetries.

The classical limit of  $\hat{H}_S$ , corresponding to  $S \rightarrow \infty$ , is obtained by replacing the spin operators with their expectation values over  $SU(2)$  spin coherent states  $|\Omega(\theta, \varphi)\rangle$ , which represent points on the unit sphere  $S^2$  parametrized by the polar and azimuthal angles  $\theta$  and  $\varphi$ . In other words we substitute  $\hat{\mathbf{S}}_j \rightarrow \mathbf{S}\mathbf{n}_j = S(\sin \theta_j \cos \varphi_j, \sin \theta_j \sin \varphi_j, \cos \theta_j)$ . Since the Dzyaloshinskii–Moriya interaction favors spin alignment in the plane perpendicular to  $\hat{z}$ , the polar angle can be fixed to  $\theta = \pi/2$ , leading to a configuration of the form  $\mathbf{S}\mathbf{n}_j = S(\cos \varphi_j, \sin \varphi_j, 0)$ . For small pitch angles,  $|\varphi_{j+1} - \varphi_j| \ll 1$ , it is possible to take the long-wavelength (continuum) limit of the lattice model. In this regime, the system is effectively described by a static chiral sine-Gordon model for the angular field variable  $\varphi = \varphi(x)$ , with the Hamiltonian density given by

$$\mathcal{H}_{SG} = JS^2 a \left[ \frac{1}{2} (\partial_x \varphi)^2 - q_0 \partial_x \varphi + m^2 (1 - \cos \varphi) \right]. \quad (2)$$

Here  $q_0 \equiv a^{-1} D/J$  is the wave number of the zero-field spiral,  $a$  the lattice parameter,  $m^2 \equiv H/JSa^2$  and the Hamiltonian is  $H_{SG} = \int dx \mathcal{H}$ . A constant  $m^2$  was added to make the energy of the uniform vacuum state equal to zero. The Hamiltonian functional in Eq. 2 is minimized by solving for the extreme condition  $\delta \mathcal{H} = 0$ ,

$$\frac{d}{dx} \frac{\partial \mathcal{H}}{\partial (\partial_x \varphi)} - \frac{\partial \mathcal{H}}{\partial \varphi} = 0 \quad (3)$$

The variational equation is satisfied by the solutions of the static sine-Gordon equation,

$$\frac{d^2 \varphi}{dx^2} = m^2 \sin \varphi \quad (4)$$

Clearly, in the absence of a magnetic field ( $m = 0$ ), the ground state is a chiral helix [15] given by  $\varphi(x) = q_0 x + cte.$ , with the sign of  $q_0$  determining the helix chirality.

As pointed out in the Introduction, the sine-Gordon model is one of the few exactly solvable field theories, possessing a rich spectrum of analytical solutions that have been extensively studied in various contexts [6, 11, 12, 17, 24, 25]. Below, we summarize the properties that are most relevant to our purposes, closely following Ref. [17].

When an external magnetic field is applied ( $m \neq 0$ ), the chiral helical ground state evolves into a *chiral soliton lattice* (CSL). This phase emerges from the competition between the exchange and Dzyaloshinskii–Moriya

interactions, which favor a uniform spiral, and the transverse magnetic field, which tends to align the spins along a fixed direction within the spiral's polarization plane. These competing tendencies gives rise to a periodic array of chiral solitons that interpolate between locally field-polarized regions, forming a nonuniform spiral whose periodicity is determined by the balance of these interactions. The chiral soliton lattice is described by

$$\varphi(x) = 2\text{am}(\bar{x}) + \pi, \quad (5)$$

where  $\bar{x} = (m/\kappa)x$  and  $\text{am}$  denotes Jacobi's amplitude function with elliptic modulus  $0 < \kappa < 1$ . By substituting Eq. 5 into the spin components and applying trigonometric identities, we obtain  $S\mathbf{n} = S(2\text{sn}^2(\bar{x}) - 1, -2\text{sn}^2(\bar{x})\text{cn}^2(\bar{x}), 0)$ . For sufficiently strong external fields, the fully polarized (FP) state ( $\varphi = 0$ ) becomes the ground state. The magnetization along the field direction given by:

$$M^x = S \left( \frac{2}{\kappa^2} - \frac{2E}{\kappa^2 K} - 1 \right), \quad (6)$$

where  $K \equiv K(\kappa)$  and  $E \equiv E(\kappa)$  are the complete elliptic integrals of the first and second kinds, respectively [17]. The elliptic modulus  $\kappa$  is related to the external magnetic field through  $\kappa = \frac{4E}{\pi q_0} \sqrt{\frac{H}{JSA^2}}$  [17]. As shown in Fig. 2 (a), the magnetization curve exhibits a distinctive profile—most notably, it evolves continuously with the applied field approaching saturation with infinite derivative.

The magnetization is directly related to the number of solitons because “addition” of a single soliton to the fully polarized (FP) state reduces the total magnetization by a finite amount  $\Delta M^x = M_{\text{FP}}^x - M_{\text{sol}}^x$ . The continuity of the magnetization curve thus indicates that the density of chiral solitons is suppressed at the quantum critical point  $H_c$  [17]:

$$H_c = \left( \frac{\pi D}{4aJ} \right)^2 JSA^2. \quad (7)$$

This continuous evolution stands in sharp contrast to other topological spin systems—such as conventional skyrmion crystals—where the field-driven transition from a topological to a polarized phase is first order, and the density of topological solitons cannot be reduced continuously.

In the present case, the field-induced commensurate-incommensurate transition of the classical model is continuous and reflects the gradual suppression of the soliton density with increasing magnetic field. In the quantum regime, this transition is replaced by a continuous quantum phase transition between a Tomonaga–Luttinger liquid and a gapped, fully polarized phase. The corresponding quantum critical behavior is governed by the softening of a chiral soliton mode as the system approaches the transition from the fully polarized side.

At  $H = H_c^-$ , the ground state hosts a single soliton described by the sine-Gordon solution,

$$\varphi_\tau(x) = \tau 4 \arctan \left[ e^{m(x-x_0)} \right], \quad (8)$$

where the plus sign corresponds to a soliton ( $\tau = +1$ ) and the minus sign to an antisoliton ( $\tau = -1$ ) configuration. The field profile,  $\varphi$ , is presented in Fig. 2 (b), while Fig. 1 illustrates the associated spin configuration. Solitons have lower energy than anti-solitons due to the presence of the DM term in Eq. (1). To verify that our definition is consistent with this condition, consider a spin at site  $i$  pointing along the  $x$ -axis and another spin at site  $j$  rotated around the  $z$ -axis. The corresponding DM energy contribution is  $\sim -\sin \varphi$ . For the excitation to lower the energy, we require  $\varphi > 0$ , which corresponds to a counterclockwise rotation (with  $\varphi$  measured from the  $x$ -axis under the standard convention). Since our operator produces precisely this type of rotation, we conclude that it generates excitations with the energetically preferred chirality.

The size of the soliton is determined by the magnetization it carries with respect to the fully polarized (FP) state. Specifically,

$$\Delta M^x = S \int_{-\infty}^{\infty} [1 - \cos \varphi_\tau(x)] dx = \frac{4S}{m}, \quad (9)$$

where  $\Delta M^x$  denotes the corresponding change in magnetization. The characteristic length is therefore  $\ell_s(H) = \Delta M^x / S = 4/m(H)$ , making explicit its dependence on the external magnetic field  $H$ .

Due to the effective easy-plane anisotropy, the projection of the spin configuration onto the  $xy$  plane establishes a mapping  $f : S^1 \rightarrow S^1$  in the continuum limit. Here, the base manifold  $S^1$  corresponds to the spatial coordinate of a chain with periodic boundary conditions for spins. The target manifold  $S^1$  represents the possible orientations of the spin projections in the  $xy$  plane. The net soliton charge  $\mathcal{C}$  is determined by the topological degree of this mapping, which corresponds to the winding number (or the fundamental homotopy group  $\pi_1(S^1) \cong \mathbb{Z}$ ). The density of topological charge is given by:

$$\mathcal{Q}(x) \equiv \frac{1}{2\pi} \partial_x \varphi, \quad (10)$$

and the total topological charge is  $\mathcal{C} \equiv \frac{1}{2\pi} \int_{-\infty}^{\infty} \partial_x \varphi(x) dx = \frac{1}{2\pi} [\varphi(\infty) - \varphi(-\infty)]$ , Fig. 2 (c) sketches the topological charge density. It is immediately apparent that the term in the Hamiltonian density Eq. 2 arising from the DM interaction, which involves a first spatial derivative of the field  $\varphi$ , can be interpreted as a chemical potential coupled to the topological charge  $\mathcal{C}$ . Individual soliton/antisoliton solutions given in Eq. (8) result in  $\mathcal{C} = \tau$ .

Returning to the lattice formulation, the underlying physics remains essentially the same as in the continuum

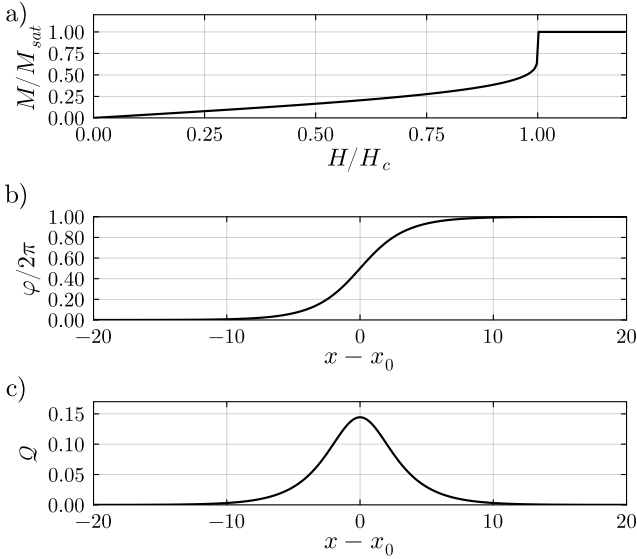


FIG. 2. a) Field dependence of the magnetization. b) Spatial profile of the soliton solution  $\varphi_+(x)$  in units of  $2\pi$ . c) Spatial profile of the topological charge density  $Q(x)$  associated with a single soliton at the critical field  $H = H_c$ .

limit [17]. On a discrete chain, the winding number associated with a given spin configuration can be computed through a geodesic interpolation,

$$\mathcal{C} \equiv \frac{1}{2\pi} \sum_{i=1}^L \arcsin [\hat{x} \cdot (\mathbf{S}_i \times \mathbf{S}_{i+1})], \quad (11)$$

where the identification  $L + 1 \equiv 1$  enforces periodic boundary conditions,  $\mathbf{S}_{L+1} = \mathbf{S}_1$ . These boundary conditions are essential for  $\mathcal{C}$  to be well-defined, since the base manifold must be topologically equivalent to  $S^1$ . From this point onward, we assume periodic boundary conditions throughout. The sign of the topological charge carried by each soliton is fixed by the chirality imposed by the Dzyaloshinskii–Moriya interaction, and the total number of solitons in the system is simply given by  $N_s = |\mathcal{C}|$ .

As mentioned in the Introduction, a central goal of this work is to explore the physics near the quantum critical point, with particular emphasis on the character of the low-energy excitations. For  $H > H_c$ , the system is fully polarized and the classical elementary excitations correspond to spin waves with a gapped dispersion centered at  $k = 0$ , as presented in Fig. 3. The magnon dispersion is given by:

$$\omega(k) = -J [\cos(ka) - 1] + H. \quad (12)$$

At the critical field  $H = H_c$ , the spin-wave spectrum remains gapped, with a gap  $\Delta E = H_c$ . This behavior reflects the fact that the commensurate–incommensurate transition is not driven by the softening of a magnon mode, as in conventional magnetically ordered sys-

tems [26], but rather by the condensation of chiral solitons. In the classical limit, the resulting CSL and the spiral magnetic state represent distinct types of order. However, once quantum fluctuations are included, both phases evolve into a Tomonaga–Luttinger liquid (TLL), and the distinction between them becomes less pronounced. As will be shown later, these two scenarios can nevertheless be clearly discriminated in the quantum regime by analyzing the nature of the low-energy excitations for  $H \gtrsim H_c$ . In this regime, the QCP marks the softening of a chiral soliton mode that drives the transition between the TLL and the fully polarized phase.

We now specify the parameter regime of our study. Since our objective is to investigate emergent solitonic physics, we focus on configurations in which solitons extend over several lattice sites, ensuring a clear distinction from magnons, which remain localized on the scale of a single site. In other words, we target the mesoscopic regime, defined by  $a < \ell_s \ll L$ , where  $a$  is the lattice spacing,  $\ell_s$  the soliton size. For comparison, the semi-classical regime—considered a limiting case of the mesoscopic one—corresponds to  $a \ll \ell_s \ll L$ , where quantum corrections are perturbative and the soliton mass remains much larger than the magnon mass. To access the mesoscopic regime in our simulations, we set  $J = 1$  and  $D = 1/\sqrt{3}$ . This choice allows us to study system sizes that are both computationally tractable and large enough to capture the essential solitonic behavior. The qualitative features discussed in the following are robust across a wide range of  $D$  values.

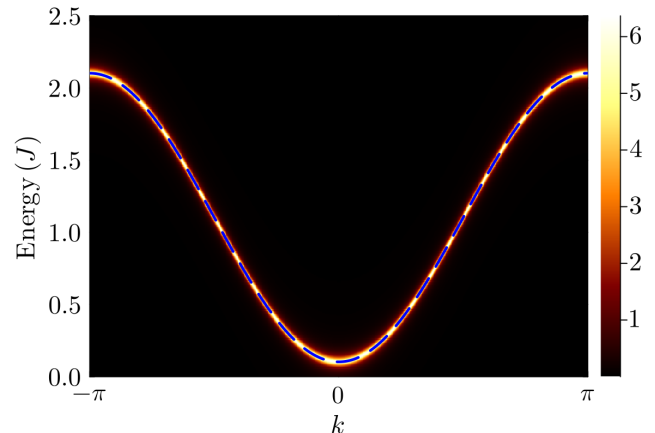


FIG. 3. Dynamical spin structure factor and magnon dispersion (blue dashed line) obtained from Linear Spin Wave Theory (LSWT) calculations. The spectral intensities were computed using `Sunny.jl` library (v0.7) [27].

### III. QUANTIZATION AND S-DUALITY

The profound connection between the bosonic quantum sine-Gordon model and the fermionic Thirring model is based on the identification of the soliton and an-

tisoliton excitations of the quantum sine-Gordon model with the single-particle fermions of the Thirring model. It maps the C-IC transition of the sine-Gordon model to the metal-insulator transition of the Thirring model driven by the chemical potential. Here we summarize its key steps (the detailed mapping is described in Appendix A).

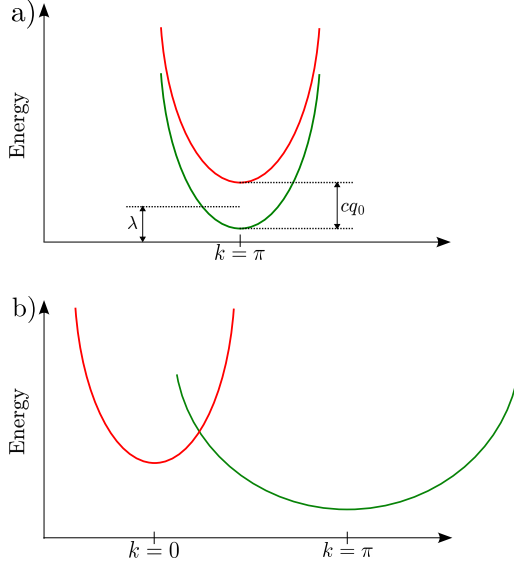


FIG. 4. a) Schematic representation of the fermionic soliton and antisoliton bands in the massive Thirring model, both featuring minima at  $k = \pi$  and possessing identical effective masses. The sine-Gordon vacuum corresponds to the half-filled case, where the chemical potential lies within the band gap ( $c|q_0| < 2\lambda$  in Eq. (19)) and energies of solitons and antisolitons are positive. (b) Same as in (a), but for the effective lattice model Eq. (51), where the dispersion minima occur at different momenta ( $k = \pi$  for the soliton band and  $k = 0$  for the antisoliton band) and the effective masses are not equal (the soliton mass is significantly larger than that of the antisoliton).

We quantize the classical sine-Gordon model, whose continuum Hamiltonian density is given by:

$$\mathcal{H} = JS^2 a \left( \frac{1}{2} (\partial_x \theta)^2 + \frac{1}{2} \sin^2 \theta (\partial_x \varphi)^2 + q_0 \sin^2 \theta \partial_x \varphi - m^2 \sin \theta \cos \varphi \right), \quad (13)$$

via Lagrangian formalism,

$$L = \int dx \left( \frac{S}{a} (\cos \theta - 1) \dot{\varphi} - \mathcal{H} \right) \quad (14)$$

where the first term is the quantum Berry phase and the dot on the shifted field  $\tilde{\varphi} = \varphi - q_0 x$  denotes the time derivative  $\partial_t$ . Fields  $\theta$  and  $\tilde{\varphi}$  depend on  $x$  and  $t$ .

In the next step, we expand  $\theta$  around its classical equilibrium value,  $\theta = \pi/2 + \tilde{\theta}$ , and integrate out the quadratic fluctuations of  $\tilde{\theta}$ . After performing the corresponding algebraic manipulations and rescaling the

fields, we obtain the effective quantum sine-Gordon Hamiltonian density,

$$\mathcal{H}_{\text{SG}} = \frac{c\kappa}{2} \Pi^2 + \frac{c}{2\kappa} (\partial_x \varphi)^2 - \frac{cq_0}{\sqrt{4\pi\kappa}} \partial_x \varphi - \frac{HS}{a} \cos[\sqrt{4\pi}\varphi]. \quad (15)$$

Here,  $\Pi$  denotes the canonical momentum conjugate to the field  $\varphi$ , satisfying  $[\varphi(x, t), \Pi(x', t)] = i\delta(x - x')$ , and the parameter  $\kappa$  is defined in Eq. (A11). Equation Eq. (15) corresponds to the quantum sine-Gordon model describing the dynamics of kink excitations (solitons and antisolitons).

A remarkable discovery by Coleman [13] and Mandelstam [14], and, independently, by Luther and Emery [28], is that Eq. (15) can be exactly mapped to the Thirring model of massive Dirac fermions. The mapping is based on the observation that the exponential operator,

$$O(x) = e^{i\zeta \int_{-\infty}^x dx' \Pi(x')} \quad (16)$$

creates a soliton of height  $\zeta$  centered at  $x$ . This is proven with the help of the operator identity  $[A, e^B] = Ce^B$  which holds if  $C = [A, B]$  commutes with both  $A$  and  $B$ . Applied to our situation, the identity,

$$[\varphi(y), O(x)] = -\zeta \Theta(x - y) O(x) \quad (17)$$

means that the action of  $O(x)$  on an eigenstate  $|\varphi\rangle$  of the operator  $\hat{\varphi}$ , changes it to the state  $|\varphi'\rangle$  with the eigenvalue  $\varphi(y) - \zeta \Theta(x - y)$  which is exactly the kink of height  $\zeta$  at position  $x$ .

This point underlies the bosonization ‘miracle.’ As shown in Appendix A, the operator

$$\psi_{\pm}^{\dagger}(x) = \frac{1}{\sqrt{2\pi\alpha}} \exp \left[ \mp i\sqrt{\pi}(\varphi(x) \mp \int_{-\infty}^x dx' \Pi(x')) \right] e^{-ip_0 x} \quad (18)$$

creates right- and left-moving Dirac fermions with the correct Fermi statistics [14]. Notice that  $\psi_{\pm}$  contains the exponential soliton operator of Eq. (16) with  $\zeta = \sqrt{\pi}$ , implying that these fermions are precisely the quantum solitons of the sine-Gordon field  $\varphi$  appearing in Eq. (15).

The remarkable feature of Eq. (18) is the emergence of a finite momentum shift

$$p_0 = \frac{2\pi S}{a},$$

which distinguishes integer- from half-integer-spin chains. For integer  $S$ , the soliton dispersion minimum is located at the Brillouin-zone origin because  $p_0 = (2\pi/a) \times \text{integer} \equiv 0$ . In contrast, for half-integer  $S$ , the soliton band minimum is shifted to the zone boundary,  $p_0 \sim \pi/a$ . This topological spin-parity effect originates from the Berry-phase term in Eq. (14) and was previously obtained in the instanton analysis of the quantum sine-Gordon model [29, 30]. Our lattice-based calculation of the soliton dispersion, together with the DMRG results presented in the next sections, provides a direct and independent confirmation of this striking prediction.

Subsequent steps of the bosonization technology are well-documented [see e.g. [25] and Appendix A] and provide a rigorous way to map the sine-Gordon Hamiltonian Eq. (15) to a massive Thirring model (mT), i.e., a Thirring model with massive Dirac fermions Eq. (A18).

The fermionic formulation of the problem becomes particularly transparent at the special value  $\kappa = 1$ , known as the Luther–Emery point [28], where the mapping yields a noninteracting Hamiltonian that can be readily diagonalized. In this limit, the Hamiltonian describes two independent fermionic bands,

$$H_{\text{mT}}^{\kappa=1} = \sum_k \epsilon_k (u_k^\dagger u_k + h_k^\dagger h_k) - \frac{cq_0}{2} (u_k^\dagger u_k - h_k^\dagger h_k), \quad (19)$$

where  $k$  is measured from  $p_0$ ,  $\epsilon_k = \sqrt{c^2 k^2 + \lambda^2}$  is the dispersion relation of solitons and anti-solitons,  $\lambda = HS\alpha/a$  is the mass gap in the fermion spectrum and positive (negative)  $q_0$  plays the role of chemical potential that adds solitons  $u_k^\dagger$  (antisolitons  $h_k^\dagger$ ) to the system provided  $c|q_0| > 2\lambda$  [31].

It is worth noting the emergence of a  $U(1)$  symmetry in the effective low-energy Hamiltonian Eq. (19), which captures the commensurate–incommensurate transition of the lattice spin model Eq. (1).

#### IV. QUANTUM SOLITONS

We now turn to the description of quantum solitons in the lattice model  $\hat{H}_S$ . Our starting point is an operator that creates a classical soliton—represented as a product state—when acting on the fully polarized reference state. Quantum fluctuations are incorporated through a *momentum-space (Bloch-space) orthogonalization* procedure, analogous to the construction of Wannier orbitals: the soliton states are first normalized in momentum space and then transformed back to real space. This method produces a set of mutually orthogonal soliton states, enabling us to compute the quantum tunneling of a soliton between different lattice sites. We emphasize that these “Wannierized” soliton states are no longer product states; the orthogonalization procedure necessarily generates entanglement in the spin degrees of freedom.

Within this framework, we can then formulate an effective tight-binding Hamiltonian, which makes explicit how quantum fluctuations generate soliton delocalization and thereby enrich the system’s low-energy dynamics.

Finally, we compare the predictions of this semiclassical framework with the quantum dynamics obtained using Time-Evolving Block Decimation (TEBD) techniques and discuss the relevance of these results for potential inelastic neutron scattering experiments.

##### A. Soliton operator

As shown in Appendix B, the exact ground state for  $H \geq H_c$  is the fully polarized configuration along the  $\hat{x}$

direction. Since this state contains no solitons, we refer to it as the *vacuum state* and denote it by

$$|0\rangle \equiv \bigotimes_l |\rightarrow\rangle_l, \quad (20)$$

where  $|\rightarrow\rangle_l = (|\uparrow\rangle_l + |\downarrow\rangle_l)/\sqrt{2}$  is the maximal-weight eigenstate of the operator  $\hat{S}_l^x$ .

The operators that create a *classical* soliton ( $\tau = +1$ ) or anti-soliton ( $\tau = -1$ ) centered at site  $j$  on top of the fully polarized ground state are:

$$\hat{T}_{j\tau}^\dagger \equiv (\hat{S}_j^z + i\hat{S}_j^y) \prod_{l \neq j} \exp\left\{-i\varphi_\tau(l-j)\hat{S}_l^z\right\}. \quad (21)$$

The corresponding annihilation operators are,

$$\hat{T}_{j\tau} = \prod_{l \neq j} \exp\left\{i\varphi_\tau(l-j)\hat{S}_l^z\right\} (\hat{S}_j^z - i\hat{S}_j^y). \quad (22)$$

As expected, these operators annihilate the vacuum:  $\hat{T}_{j\tau} |0\rangle = 0$ . In terms of the local spin degrees of freedom, the creation operators  $\hat{T}_{j\tau}^\dagger$  rotate the spins around the  $\hat{z}$ -axis by the angle  $\varphi_\tau(x)$  given by Eq. (8), which corresponds to the profile of the single-soliton (or anti-soliton) solution of the classical sine-Gordon Hamiltonian Eq. (2) for  $m^2 = H/(JSd^2)$ . To properly account for periodic boundary conditions, we define  $x \equiv (l - j + L/2) \pmod{L} - L/2$ .

As shown in Appendix C, the operators  $\{\hat{T}_\tau^\dagger, \hat{T}_\tau, \hat{S}^x\}$  satisfy the following commutation relations:

$$\begin{aligned} [\hat{T}_{j'\tau}, \hat{T}_{j\tau}^\dagger] &= 2\tilde{\delta}_{j'j\tau} \hat{S}_j^x, \\ [\hat{T}_{j\tau}^\dagger, \hat{S}_j^x] &= 2\hat{T}_{j\tau}^\dagger, \\ [\hat{T}_{j\tau}, \hat{S}_j^x] &= -2\hat{T}_{j\tau}, \end{aligned} \quad (23)$$

where the function  $\tilde{\delta}_{j'j\tau}$  plays the role of an approximate Kronecker delta in a coarse-grained description. Equivalently, upon choosing the soliton size as the unit of length, the set  $\{\hat{T}_\tau^\dagger, \hat{T}_\tau, \hat{S}^x\}$  provides an approximate realization of the  $\mathfrak{su}(2)$  Lie algebra.

As follows from the algebraic structure, the  $\hat{T}$ -operators obey bosonic-like commutation relations. In a coarse-grained description, solitons can therefore be interpreted as hard-core bosons. Moreover, in the dilute limit, that is, when the soliton density is sufficiently small, this identification becomes exact.

##### B. Quantum soliton operator: Wannierization of the soliton operator

A drawback of the operators  $\hat{T}_{j\tau}$  introduced above is that the single-particle states  $\hat{T}_{j\tau}^\dagger |0\rangle = |\varphi_\tau^{(j)}\rangle$  that they generate

$$|\varphi_\tau^{(j)}\rangle = \bigotimes_l \frac{1}{\sqrt{2}} \left( e^{-i\varphi_\tau(l-j)/2} |\uparrow\rangle_l + e^{i\varphi_\tau(l-j)/2} |\downarrow\rangle_l \right) \quad (24)$$

are not mutually orthogonal,

$$\langle \varphi_\tau^{(j)} | \varphi_\tau^{(j')} \rangle = \prod_{l=1}^L \cos \left[ \frac{\varphi_\tau(l-j) - \varphi_\tau(l-j')}{2} \right] \neq \delta_{jj'}, \quad (25)$$

for  $j, j' = 1, \dots, L$ . By using a standard Wannierization procedure, we can construct a new set of single-particle orthonormal states  $\{\hat{\mathfrak{T}}_{j\tau}^\dagger |0\rangle\}$  given by:

$$\hat{\mathfrak{T}}_{j\tau}^\dagger |0\rangle \equiv \frac{1}{\sqrt{L}} \sum_{k \in 1\text{BZ}} e^{-ikj} \frac{\hat{T}_{k\tau}^\dagger}{\|\hat{T}_{k\tau}^\dagger |0\rangle\|} |0\rangle, \quad (26)$$

where,

$$\hat{T}_{k\tau}^\dagger = \frac{1}{\sqrt{L}} \sum_{l=1}^L e^{ikl} \hat{T}_{l\tau}^\dagger \quad (27)$$

is the Fourier transform of the soliton operator with  $k \in [-\pi, \pi]$ . Eq. 26 can be rewritten in the form:

$$\begin{aligned} \hat{\mathfrak{T}}_{j\tau}^\dagger |0\rangle &= \frac{1}{\sqrt{L}} \sum_k e^{-ikr} \frac{\hat{T}_{k\tau}^\dagger |0\rangle}{\|\hat{T}_{k\tau}^\dagger |0\rangle\|} \\ &= \sum_{l=1}^L \left( \frac{1}{L} \sum_k \frac{e^{-i(j-l)k}}{\|\hat{T}_{k\tau}^\dagger |0\rangle\|} \right) \hat{T}_{l\tau}^\dagger |0\rangle \quad (28) \\ &\equiv \sum_{l=1}^L w_{j-l\tau} \hat{T}_{l\tau}^\dagger |0\rangle. \end{aligned}$$

From the last term, it is evident that the coefficients,

$$w_{j-l\tau} = \frac{1}{L} \sum_k \frac{e^{-i(j-l)k}}{\|\hat{T}_{k\tau}^\dagger |0\rangle\|}, \quad (29)$$

represent the components of the “Wannerized” operator in the original basis spanned by the  $\hat{T}_{j\tau}^\dagger$ -operators.

The norm of the Fourier-transformed soliton operator,  $N_{k\tau} \equiv \|\hat{T}_{k\tau}^\dagger |0\rangle\|$ , can be evaluated analytically:

$$\begin{aligned} N_{k\tau}^2 &= \frac{1}{L} \sum_{l,l'=1}^L e^{-ik(l-l')} \prod_p \cos \left[ \frac{\varphi_\tau(p-l) - \varphi_\tau(p-l')}{2} \right] \\ &= \sum_{l=1}^L e^{-ikl} \prod_p \cos \left[ \frac{\varphi_\tau(p) - \varphi_\tau(p-l)}{2} \right], \quad (30) \end{aligned}$$

where, in the second line, we have used translation invariance of the chain (i.e., periodic boundary conditions).

Let us reflect on the previous construction. We began with a well-localized sine–Gordon soliton (or anti-soliton) creation operator  $\hat{T}_{j\tau}^\dagger$ . Through a Wannierization procedure, we constructed a new set of operators as linear combinations of solitons centered at all sites,

$$\hat{\mathfrak{T}}_{j\tau}^\dagger = \sum_{l=1}^L w_{j-l\tau} \hat{T}_{l\tau}^\dagger, \quad (31)$$

with coefficients  $w_{j-l\tau}$  that, formally, are the overlaps  $w_{j-l\tau} \propto \langle 0 | \hat{\mathfrak{T}}_{j\tau} \hat{T}_{l\tau}^\dagger | 0 \rangle$ . As shown in Appendix D, these overlaps decays exponentially,  $w_{j-j'} \sim e^{-2m|j-j'|}$  for large separation  $|j - j'|$ .

The Wannier-like operators create a soliton wave packet centered at site  $j$  that incorporates quantum delocalization via the generation of entangled single-soliton states that are orthogonal for solitons centered around different sites. By contrast, the bare states generated by  $\hat{T}_{j\tau}^\dagger |0\rangle$  are non-orthogonal product states. The structure of the “Wannerized” soliton state is sketched in Fig. 5. Henceforth—with a slight abuse of terminology—we refer to these objects as *quantum solitons*, since their strongly localized wave packets still support a quasiparticle interpretation. Equivalently, the Wannierization procedure furnishes a variational construction of the single-soliton states of the spin- $\frac{1}{2}$  chain. Related “quantum skyrmion” operators have been introduced in Refs. [32–34]; similarities and differences with our construction are discussed in Sec. VII.

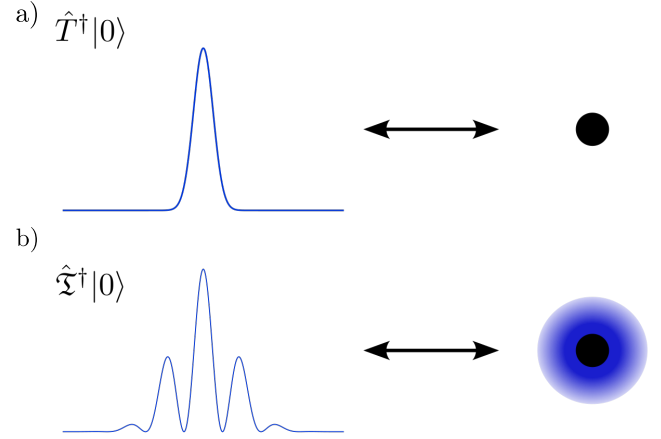


FIG. 5. Schematic representation of the action of the soliton operator (a) and the Wannerized soliton operator (b).

### C. Soliton kinematics

Before addressing the dynamics and deriving an effective model for the solitons, let us first analyze their kinematic properties. The Fourier transform of the Wannerized soliton operator is simply given by:

$$\hat{\mathfrak{T}}_{k\tau}^\dagger |0\rangle = \frac{1}{\|\hat{T}_{k\tau}^\dagger |0\rangle\|} \hat{T}_{k\tau}^\dagger |0\rangle, \quad (32)$$

that is, the normalized Fourier transform of the classical soliton operator. As expected, the solitons (antisolitons) carry a finite magnetization along the  $x$ -direction,  $\Delta M_{\tau k}^x = M_{\text{FP}}^x - M_{\tau k}^x$ , which varies continuously with the momentum  $k$  as presented in Fig. 6 (a). More interestingly, the solitons carry a finite magnetization component

$M_{\tau k}^z$  along the  $z$ -axis (the DM direction), with a sign set by the sign of momentum, see Fig. 6 (b). At the special (inversion-symmetric) momenta  $k = 0$  and  $k = \pi$ , however, a mirror symmetry about the mid-point of a bond, which maps  $x \rightarrow -x$ ,  $k \rightarrow -k$  and  $S^x \rightarrow S^x, S^{y,z} \rightarrow -S^{y,z}$ , forces this magnetization to vanish. Namely, this symmetry relates  $(k, M^z) \leftrightarrow (-k, -M^z)$  and guarantees a symmetric spectrum  $E(k) = E(-k)$ .

An analogous behavior holds for the antisoliton branch [see Fig. 6 (b)], with the opposite sign of the  $z$ -magnetization at a given  $k$ . This momentum-dependent polarization sharply contrasts with single-magnon excitations, whose magnetization along the field-axis is fixed and essentially  $k$ -independent.

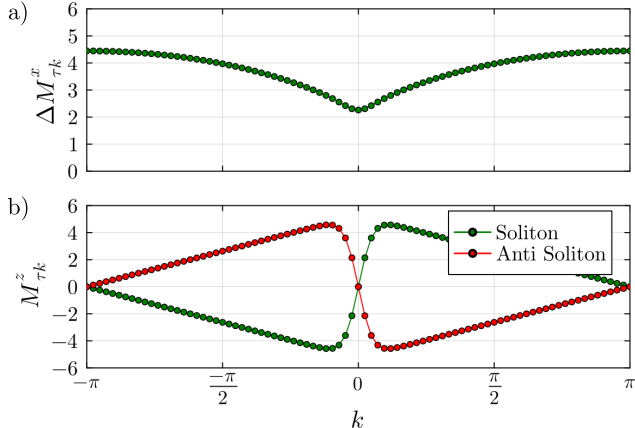


FIG. 6. Field-induced magnetization of soliton (green) and antisoliton (red). (a): Longitudinal magnetization difference  $\Delta M_{\tau k}^x$  as a function of momentum  $k$ . Only the soliton branch is shown, as the antisoliton results are identical. (b): Transverse magnetization  $M_{\tau k}^z$  along the DM direction. The quantity  $M_{\tau k}^z$  changes sign with the momentum and vanishes at  $k = 0$  and  $k = \pi$ . This calculations are at  $H = 0.11$ .

#### D. Effective tight-binding Hamiltonian

Assume now that the chain hosts a single soliton centered at site  $j$ . Since it is a quantum mechanical soliton, it can tunnel to the neighboring sites. The tunneling or hopping amplitude between sites  $j$  and  $j'$  is given by the matrix element:

$$t_{jj'\tau} = \langle \Phi_{\tau}^{(j)} | \hat{H}_S | \Phi_{\tau}^{(j')} \rangle, \quad (33)$$

with  $|\Phi_{\tau}^{(j)}\rangle = \hat{\mathcal{X}}_{j\tau}^{\dagger} |0\rangle$ . By substituting Eq. (28) into the previous expression, we obtain,

$$t_{jj'\tau} = \sum_{l,l'=1}^L w_{l'-j\tau}^* w_{j'-l\tau} \langle \varphi_{\tau}^{(l')} | \hat{H}_S | \varphi_{\tau}^{(l)} \rangle. \quad (34)$$

The explicit form of these hopping amplitudes is obtained by inserting the expressions of the Wannier coefficients

$w_{l-n\tau}$  given in Eq. (29) and reordering the factors:

$$t_{jj'\tau} = \frac{1}{L^2} \sum_{k,k'} \frac{e^{-ik'j} e^{-ikj'}}{N_{k\tau} N_{k'\tau}} \sum_{l,l'=1}^L e^{ik'l'} e^{ikl} \langle \varphi_{\tau}^{(l')} | \hat{H}_S | \varphi_{\tau}^{(l)} \rangle. \quad (35)$$

Now, we can exploit the translational invariance of  $\hat{H}_S$  by defining  $\langle \varphi_{\tau}^{(l')} | \hat{H}_S | \varphi_{\tau}^{(l)} \rangle \equiv h_{\tau}(n - n')$ , then

$$\begin{aligned} \sum_{l,l'=1}^L e^{ikl} e^{ik'l'} h(l - l') &= \sum_{s=1}^L h_{\tau}(s) e^{iks} \sum_{s'=1}^L e^{i(k+k')s'} \\ &= L \sum_s h_{\tau}(s) e^{iks} \delta_{k,-k'}, \end{aligned} \quad (36)$$

to obtain:

$$t_{jj'\tau} = \frac{1}{L} \sum_k \frac{e^{ik(j-j')}}{N_{k\tau}^2} \sum_s h_{\tau}(s) e^{iks} = \frac{1}{L} \sum_k \frac{e^{ik(j-j')}}{N_{k\tau}^2} \tilde{h}_{\tau}(k) \quad (37)$$

where  $\tilde{h}_{\tau}(k) = \sum_s h_{\tau}(s) e^{iks}$  is the Fourier transform of  $h(s)$ . In conclusion,

$$t_{\delta\tau} = \frac{1}{L} \sum_k \frac{\tilde{h}_{\tau}(k)}{N_{k\tau}^2} e^{ik\delta} \quad (38)$$

with  $\delta = j - j'$ , are the hopping amplitudes of the quantum chiral soliton. The next step is to evaluate the matrix elements  $h_{\tau}(s)$ . Since the resulting expression is lengthy and offers no direct physical insight, we defer this calculation to Appendix E. As shown in there, the matrix elements  $h_{\tau}(s)$  are real, implying that  $\tilde{h}_{\tau}(k) = \tilde{h}_{\tau}^*(-k)$ . This in turn implies that the hopping amplitudes  $t_{\delta\tau}$  are real.

With these hopping amplitudes, we can now construct an effective tight-binding Hamiltonian for the solitons on the chain. The last necessary ingredient is the associated soliton creation chemical potential, which can be computed as,

$$\mu_{\tau} = - \langle \Phi_{\tau}^{(j)} | \hat{H}_S | \Phi_{\tau}^{(j)} \rangle + E_0, \quad (39)$$

where  $E_0/L = -J/4 - H/2$  is the ground state energy density, and  $j$  can be any site on the chain due to the translational invariance of the Hamiltonian.

The resulting tight-binding Hamiltonian is given by:

$$\hat{H}_{\text{eff}} = \sum_{j,\delta,\tau} (t_{\delta\tau} b_{j\tau}^{\dagger} b_{j+\delta\tau} + \text{H.c.}), \quad (40)$$

where the hopping amplitudes  $t_{\delta\tau}$  and the chemical potential for each flavor,  $\mu_{\tau} = -t_{0\tau}$ , depend on the external field  $H$ . Note that the operators  $b_{\tau}$  and  $b_{\tau}^{\dagger}$  also implicitly depend on the field because the soliton size decreases with increasing  $H$ .

For periodic boundary conditions ( $L + 1 \equiv 1$ ), the Hamiltonian is diagonalized in the reciprocal space,

$$\hat{b}_{k\tau} = \frac{1}{\sqrt{L}} \sum_{l=1}^L e^{ilk} b_{l\tau}, \quad (41)$$

to obtain:

$$\hat{H}_{\text{eff}} = \sum_{k,\tau} [\omega_k^\tau - \mu_\tau] \hat{b}_{k\tau}^\dagger \hat{b}_{k\tau}, \quad (42)$$

where

$$\omega_k^\tau = \sum_{\delta=1}^n t_{\delta\tau} \cos k\delta. \quad (43)$$

The number  $n$  of neighbors retained in the calculation is determined by the decay rate of the hopping amplitudes  $|t_{\delta\tau}|$  with the separation  $\delta$ . We also note that  $\omega_k^\tau = \omega_{-k}^\tau$ , a direct consequence of the reality of the hopping amplitudes  $t_{\delta\tau} = t_{\delta\tau}^*$ .

We defer the discussion of the soliton dispersion  $\omega_k^\tau$  to the next section and conclude here by analyzing the dependence of the hopping amplitudes on the external magnetic field. Fig. 7 shows the hopping amplitudes up to fourth neighbors as a function of the field.

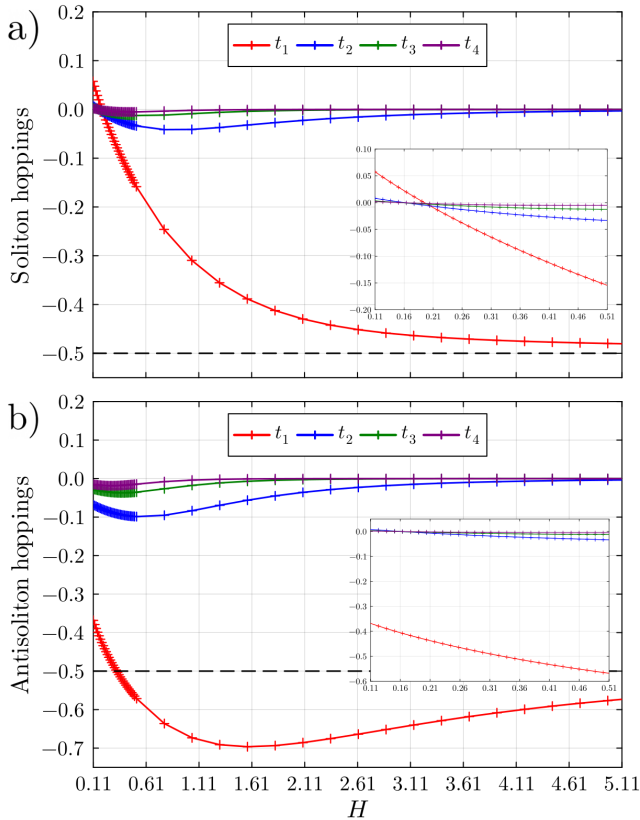


FIG. 7. Soliton (a) and anti-soliton (b) hopping amplitudes as a function of the Zeeman field. The inset in each figure is a Zoom for a small field region. The dashed line represents the single magnon hopping amplitude.

For the soliton, the nearest-neighbor hopping amplitude dominates over the entire field range, except within a narrow window around  $H = H_0 \simeq 0.2$ , where it changes sign:  $t_{1+} > 0$  for  $H < 0.2$  and  $t_{1+} < 0$  for  $H > 0.2$ . This sign reversal shifts the minimum of the soliton dispersion

from  $k = \pi$  (for  $H < 0.2$ ) to  $k = 0$  (for  $H > 0.2$ ). In addition, all hopping amplitudes are strongly suppressed near  $H \simeq 0.2$ , leading to an almost flat band. The change of sign of  $t_{1+}$  is expected, since the soliton evolves continuously into a magnon as the field increases, and the magnon dispersion attains its minimum at  $k = 0$ , as shown in Fig. 3.

In contrast, for the anti-soliton the nearest-neighbor hopping also dominates but remains negative throughout the entire field range. At higher fields, the nearest-neighbor term becomes, essentially, the only appreciable contribution for both soliton and anti-soliton, with its magnitude approaching the expected magnon-hopping value in the fully polarized limit.

While our main discussion focused on the  $S = \frac{1}{2}$  version of  $\hat{H}_S$ , Appendix F shows that the lattice formulation for arbitrary  $S$  correctly reproduces the integer/half-integer alternation of the soliton-band minimum discussed in Sec. III and reported in Ref. [30] for a particular limit of the model. This alternation is caused by a spin Berry phase [29].

### E. Jordan-Wigner transformation

Since the effective model derived in the previous section describes a dilute gas of hard-core bosons in one dimension (1D), it is convenient to employ a generalized Jordan-Wigner transformation [35], which maps hard-core bosons with two flavors ( $\tau = \pm$ ) to constrained ( $c_{j,+}^\dagger c_{j,-}^\dagger = 0$ ) spin 1/2 fermions:

$$\begin{aligned} c_{j,+} &= e^{i\pi \sum_{\ell < j} n_\ell^{(b)}} b_{j+}, & c_{j,-} &= e^{i\pi \sum_{\ell < j} n_\ell^{(b)}} b_{j-}, \\ c_{j,+}^\dagger &= b_{j+}^\dagger e^{-i\pi \sum_{\ell < j} n_\ell^{(b)}} & c_{j,-}^\dagger &= b_{j-}^\dagger e^{-i\pi \sum_{\ell < j} n_\ell^{(b)}}, \end{aligned}$$

where,

$$n_\ell^{(b)} = \sum_\tau b_{j\tau}^\dagger b_{j\tau} = n_{\ell,+}^{(c)} + n_{\ell,-}^{(c)} \equiv n_\ell^{(c)}, \quad (44)$$

and  $n_{\ell,\tau}^{(c)} \equiv c_{\ell,\tau}^\dagger c_{\ell,\tau}$ . Note that the constraint satisfied by the fermionic operators,  $c_{j,+}^\dagger c_{j,-}^\dagger = 0$ , implies that double-occupied states are excluded from the Hilbert space.

The real space effective Hamiltonian Eq. (40) can now be expressed in terms of the fermionic operators:

$$\hat{H}_{\text{eff}} = \sum_{j,\delta,\tau} t_{\delta\tau} \left[ c_{j,\tau}^\dagger \mathcal{S}_{j,\delta} c_{j\tau\delta,\tau} + \text{H.c.} \right], \quad (45)$$

with,

$$\mathcal{S}_{j,\delta} = \prod_{j \leq \ell < j+\delta} [1 - 2n_\ell^{(c)}]. \quad (46)$$

being the Jordan-Wigner string.

By separating the non-interacting part of  $\hat{H}_{\text{eff}}$  from the interaction terms, we obtain:

$$\hat{H}_{\text{eff}} = \sum_{j,\delta,\tau} \left[ t_{\delta,\tau} c_{j,\tau}^\dagger c_{j\tau\delta,\tau} + \text{H.c.} \right] + \hat{H}_{\text{eff}}^{\text{int}}, \quad (47)$$

where  $\hat{H}_{\text{eff}}^{\text{int}}$  corresponds to correlated hopping terms arising from the density operators in Eq. (46). In reciprocal space,

$$\hat{c}_{k,\tau} = \frac{1}{\sqrt{L}} \sum_{l=1}^L e^{ilk} \hat{c}_{l,\tau}, \quad (48)$$

the non-interacting part of  $\hat{H}_{\text{eff}}$  becomes diagonal,

$$\hat{H}_{\text{eff}} = \sum_{k,\tau} [\omega_k^\tau - \mu_\tau] \hat{c}_{k,\tau}^\dagger \hat{c}_{k,\tau} + \hat{H}_{\text{eff}}^{\text{int}}, \quad (49)$$

and the connection with Thirring's model with  $\kappa = 1$  becomes evident after relabeling operators:

$$u_k \equiv \hat{c}_{k,+}, \quad h_k \equiv \hat{c}_{k,-}, \quad (50)$$

which leads to,

$$\hat{H}_{\text{eff}} = \sum_{k,\tau} [\epsilon_k^+ - \mu] u_k^\dagger u_k + [\epsilon_k^- - \mu] h_k^\dagger h_k + \hat{H}_{\text{eff}}^{\text{int}}, \quad (51)$$

with,

$$\mu = \frac{\mu_+ + \mu_-}{2}, \quad \delta\mu = \frac{\mu_+ - \mu_-}{2}, \quad \epsilon_k^\pm = \omega_k^\pm \mp \delta\mu.$$

Similar to the Thirring model, the non-interacting sector of  $\hat{H}_{\text{eff}}$  describes two gapped fermions with the chemical potential determined by the magnetic field. A quantum phase transition occurs when the chemical potential reaches the bottom of the soliton band. Owing to the U(1) invariance of  $\hat{H}_{\text{eff}}$ , associated with the conservation of soliton charge, the corresponding critical point is a free-fermion fixed point ( $\kappa = 1$ ) characterized by a correlation-length exponent  $\nu = 1/2$  and a dynamical exponent  $z = 2$ , reflecting the quadratic dispersion of the free fermions.

The interaction terms in  $\hat{H}_{\text{eff}}^{\text{int}}$  are irrelevant under the renormalization group because the no-double-occupancy constraint forces them to involve spatial derivatives in the continuum limit. Beyond the critical point, however, once the bottom of the conduction band is populated and a finite fermion density develops, these interactions become marginally relevant. The system then enters a Tomonaga–Luttinger liquid phase with Luttinger parameter  $\kappa < 1$  in the presence of repulsive interactions.

While the massive Thirring model Eq. (19) and  $\hat{H}_{\text{eff}}$  Eq. (51) share the same universal low-energy physics, it is nevertheless instructive to examine their qualitative and quantitative differences. Such a comparison clarifies the role of quantum fluctuations and of the higher-order terms in the gradient expansion leading to the Sine–Gordon field theory, which are not fully

captured by traditional semiclassical treatments. As we will show in the following sections, these non-universal aspects play a crucial role in achieving a quantitative description of the soliton dynamics and in guiding the experimental characterization of the phenomena under study.

The first qualitative difference is that, in the massive Thirring model, the soliton and antisoliton have identical effective masses—their parabolic dispersions differ only by a constant vertical shift [Fig. 4(a)]. This property, which is a consequence of neglecting cubic and higher order terms in the gradient expansion of the DM interaction, is naturally absent in the lattice effective Hamiltonian  $\hat{H}_{\text{eff}}$ , where the two bands generally acquire distinct curvatures, as shown in Fig. 4(b). Moreover, the minimum of the soliton band can shift to  $k = \pi$  because the nearest-neighbor hopping amplitude becomes positive near the saturation field, as illustrated in Fig. 7. A further qualitative distinction is that the effective masses themselves exhibit a pronounced dependence on the applied field, as shown in the same figure.

Beyond these qualitative differences,  $\hat{H}_{\text{eff}}$  provides the full soliton and antisoliton dispersions across the entire Brillouin zone. As we discuss in Sec. VI, the field dependence of these dispersions is crucial for identifying experimental signatures of solitons and antisolitons, both in inelastic neutron scattering spectra and in specific-heat measurements.

## V. NUMERICAL RESULTS

Throughout this section, we present numerical results for the full quantum model to test and validate the arguments and effective theory developed in the preceding section. Although the classical picture of well-defined solitons in real space is blurred by quantum fluctuations, we show that the essential classical features survive, most notably the continuous field-driven phase transition evident in the magnetization curve. We further demonstrate that, over a finite range of magnetic fields, the lowest-lying excited states above the ground state are indeed solitons. Building on this, we compute their dynamics by evaluating a soliton-soliton dynamical correlator, which, as anticipated, is accurately captured by the soliton effective Hamiltonian constructed earlier. Finally, we discuss the implications of these soliton modes for the full spin-spin dynamical correlator.

All numerical results are obtained using Density Matrix Renormalization Group (DMRG) and Time-Evolution Block Decimation (TEBD) calculations implemented in the `ITensors.jl` library (v0.9) [36, 37] under periodic boundary conditions (PBC). Although DMRG with PBC is computationally demanding due to the rapid growth of the bond dimension, open boundary conditions (OBC) would explicitly break translational symmetry and introduce an artificial attractive potential that localizes solitons near the edges. To prevent such arti-

facts, we perform all simulations on finite rings of manageable size. Our main results correspond to systems with  $L = 48$  and  $L = 84$  sites, for which no appreciable finite-size effects are observed.

### A. Static properties

To assess the correspondence between the quantum soliton solution and the classical result presented in the previous section, we begin by examining the magnetization curve shown in Fig. 8. The agreement between the classical prediction and the quantum numerical data is remarkably good, indicating that the classical picture provides a reliable foundation for understanding the properties of the quantum soliton.

The numerically obtained saturation field,  $H_c = 0.105$ , is in very good agreement with the classical estimate  $H_c = 0.1028$  given in Eq. 7. As expected, the magnetization curve becomes progressively smoother for larger system sizes, since the discrete jumps associated with the successive addition of individual solitons diminish in relative magnitude. In the thermodynamic limit, the curve is expected to approach the smooth behavior predicted by the classical continuum solution. An important distinction, however, is that the logarithmic divergence of the slope of the classical magnetization curve as the saturation field is approached from below is replaced, in the quantum case, by a square-root divergence, reflecting the free-fermion fixed point that governs the critical behavior.

The size of the soliton at the critical field can be inferred from the height of the first magnetization jump. From the inset of Fig. 8, we estimate a soliton size  $\ell_s \approx 10a$ , corresponding to  $\Delta M^x \approx 5$ , in excellent consistency with the continuum prediction  $\Delta M^x \approx 4.36$  obtained from Eq. 9.

While the magnetization curve shows good agreement with classical predictions, it is important to emphasize that in the chiral-soliton phase the solitons become fully delocalized. As a consequence, the expectation values of the spin components develop an essentially flat spatial profile along the chain, illustrating how quantum fluctuations melt the classical soliton crystal and restore the translational invariance that is broken in the classical solution.

To further characterize the excitations, we now examine the lowest excited state above the fully saturated phase ( $H > H_c$ ). Fig. 9(a) shows the evolution of the energy gap  $\Delta = E_1 - E_0$  as a function of the magnetic field for a chain of length  $L = 48$ , where  $E_0$  and  $E_1$  denote the ground-state and first excited-state energies, respectively.

As shown in Fig. 9(a), the slope of the energy gap  $\Delta$  changes discontinuously around  $h \equiv H - H_c \approx 0.03$ , signaling the expected qualitative change in the nature of the lowest-energy excitations. This transition is further corroborated by the magnetization difference  $\Delta M_{\text{exc}}^x =$

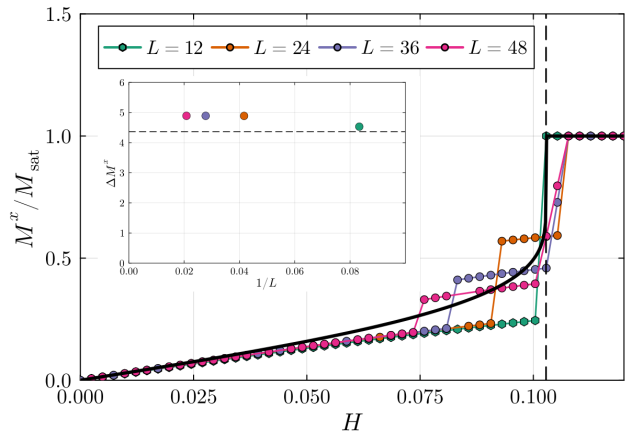


FIG. 8. Magnetization curves obtained from DMRG calculations for different system sizes. The dashed vertical line marks the critical field in the classical continuum limit, while the solid black curve represents the classical and continuum limit. Inset: absolute magnetization jump,  $\Delta M$ , as a function of the inverse system size. The dashed horizontal line shows the continuum limit prediction for classical solitons.

$M_{\text{FP}}^x - M_1^x$ , plotted in Fig. 9(b). For fields  $h > 0.03$ , the excitations carry  $\Delta M_{\text{exc}}^x = \pm 1$ , consistent with single-magnon modes. In contrast, for  $0 < h < 0.03$ , the first excited state exhibits a magnetization jump of  $\Delta M_{\text{exc}}^x \approx 5$ , consistent with the soliton size identified earlier.

We also note that the energy gap scales linearly with  $H - H_c$ , in agreement with the emergent  $U(1)$  symmetry of the free-fermion fixed point:  $\Delta \propto (H - H_c)^{\nu z}$  with  $\nu = 1/2$  and  $z = 2$ , as discussed in the previous section.

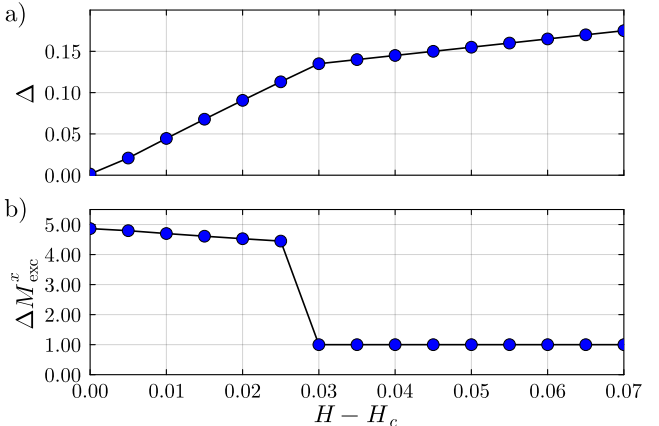


FIG. 9. Difference between the ground-state magnetization and the first excited-state magnetization  $\Delta M_{\text{exc}}^x$  (a), and the corresponding energy difference  $\Delta = E_1 - E_0$  (b) for a chain of  $L = 48$  sites, plotted as a function of the external field  $H - H_c$ , where  $H_c$  is the critical field obtained from DMRG calculations.

## B. Dynamical spin structure factor

As shown previously, for sufficiently large values of  $H$ , the lowest excitations of the system are  $S = 1$  magnons. In this regime, we expect to recover the LSWT prediction with a magnon dispersion given by Eq. 12. To test this expectation, we evaluate the real-space, real-time spin–spin correlation function,

$$\mathcal{S}^{\alpha\alpha}(j - j', t) = \langle 0 | \hat{S}_j^\alpha(t) \hat{S}_{j'}^\alpha(0) | 0 \rangle, \quad (52)$$

where  $|0\rangle$  denotes the fully polarized ground state and  $\alpha = x, y, z$ . These correlations are computed using the TEBD method, as described in Appendix G. By applying spatial and temporal Fourier transforms, we obtain the dynamical spin structure factor (DSSF),

$$\tilde{\mathcal{S}}^{\alpha\alpha}(k, \omega) = \frac{1}{2\pi L} \sum_{l, l'} \int_{-\infty}^{\infty} dt e^{i[\omega t - k(l - l')]} \mathcal{S}^{\alpha\alpha}(l - l', t). \quad (53)$$

The most relevant contributions are the transverse components with  $\alpha = y, z$ , which correspond to excitations perpendicular to the fully polarized order along the  $\hat{x}$  direction. In contrast, the longitudinal component ( $\alpha = x$ ) probes fluctuations parallel to the polarization, which are not expected in the fully polarized state. This expectation is confirmed by our numerical results, which show a negligible response in the longitudinal channel.

In Fig. 10, we present a direct comparison between the DSSF obtained from TEBD and the magnon dispersion predicted by LSWT at  $H = 5.0$ . The results show excellent agreement, demonstrating that LSWT provides a complete description of the excitation spectrum in this high-field regime.

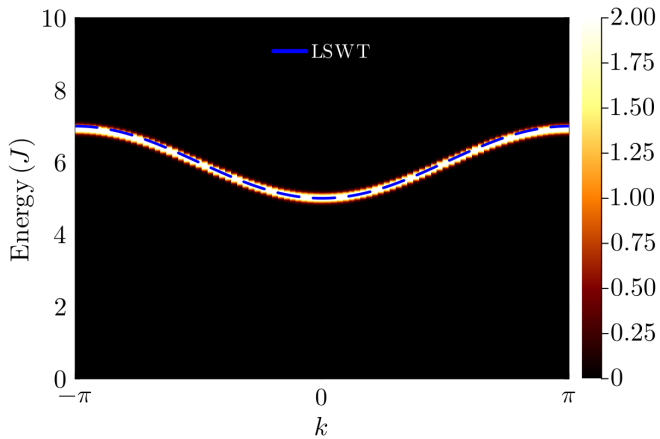


FIG. 10. DSSF for a chain of  $L = 48$  and  $H = 5 \approx 50H_c$  computed by TEBD, the blue dashed lines show the LSWT magnon dispersion. The used time step for the TEBD calculation is  $\delta t = 0.01$  with a truncation error of  $10^{-12}$  for each application of the time evolution operator, the total evolution time is  $T_f = 40$  (in units of  $J^{-1}$ ).

## C. Dynamical soliton structure factor

In Sec. IV, we introduced an effective tight-binding Hamiltonian describing the propagation of a soliton (or anti-soliton) excitation over the fully polarized background. Although this construction is based on simple physical arguments, it is crucial to test its validity by confronting its predictions with numerical results. To this end, we define the real-space and real-time *soliton-soliton* ( $\tau = +$ ) or *antisoliton-antisoliton* ( $\tau = -$ ) correlation function,

$$\mathcal{T}_\tau(j - j', t) \equiv \langle 0 | \hat{T}_{j\tau}(t) \hat{T}_{j'\tau}^\dagger(0) | 0 \rangle, \quad (54)$$

which measures the probability amplitude of finding a soliton at site  $j$  and time  $t$ , given that a soliton was created at site  $j'$  at  $t = 0$  on top of the ground state.

The corresponding dynamical soliton/antisoliton spectral function is obtained from the space–time Fourier transform of  $\mathcal{T}_\tau(j - j', t)$ ,

$$\tilde{\mathcal{T}}_\tau(k, \omega) = \frac{1}{2\pi L} \sum_{l, l'} \int_{-\infty}^{\infty} dt e^{i[\omega t - k(l - l')]} \mathcal{T}_\tau(l - l', t), \quad (55)$$

which directly encodes the soliton dispersion and lifetime. This representation provides the natural quantity for comparison with the predictions of the effective tight-binding Hamiltonian.

Here we employ the original soliton creation operator [see Eq. (21)] rather than its Wannierized form. It is worth noting that using the Wannierized form of the soliton operators in Eq. (54) would only affect the spectral weight of the  $\delta$ -function peaks in  $\tilde{\mathcal{T}}_\tau(k, \omega)$ . Since our primary interest lies in extracting the soliton dispersion relation—that is, the frequency of the peak for each value of  $k$ —from numerical calculations, and because  $\tilde{\mathcal{T}}_\tau(k, \omega)$  is not directly observable, it suffices to define  $\mathcal{T}_\tau(j - j', t)$  in terms of the non-Wannierized soliton operators.

The top panel of Fig. 11 presents the numerical results for the dynamical soliton structure factor at several values of the magnetic field, together with the soliton bands predicted by the analytical theory. The agreement is nearly perfect: the predicted soliton bands reproduce the numerically obtained dispersions with high accuracy. The apparent broadening of the numerical spectra originates primarily from the finite frequency resolution imposed by the truncation of the time evolution.

The bottom panel of Fig. 11 shows the results for the dynamical antisoliton structure factor. In contrast to the soliton case, the spectrum exhibits a more intricate structure. Although the numerically computed intensities broadly follow the analytical antisoliton dispersion, additional modes appear, reconstructing the spectrum and giving rise to richer features. These extra modes are faintly visible in the dynamical soliton structure factor for fields  $H = 0.5$  and  $1.0$  [see Figs. 11(e) and 11(d)]. This behavior provides a clear signature of hybridization between antisoliton (or soliton) modes and other excitations. In particular, because the antisoliton is always the

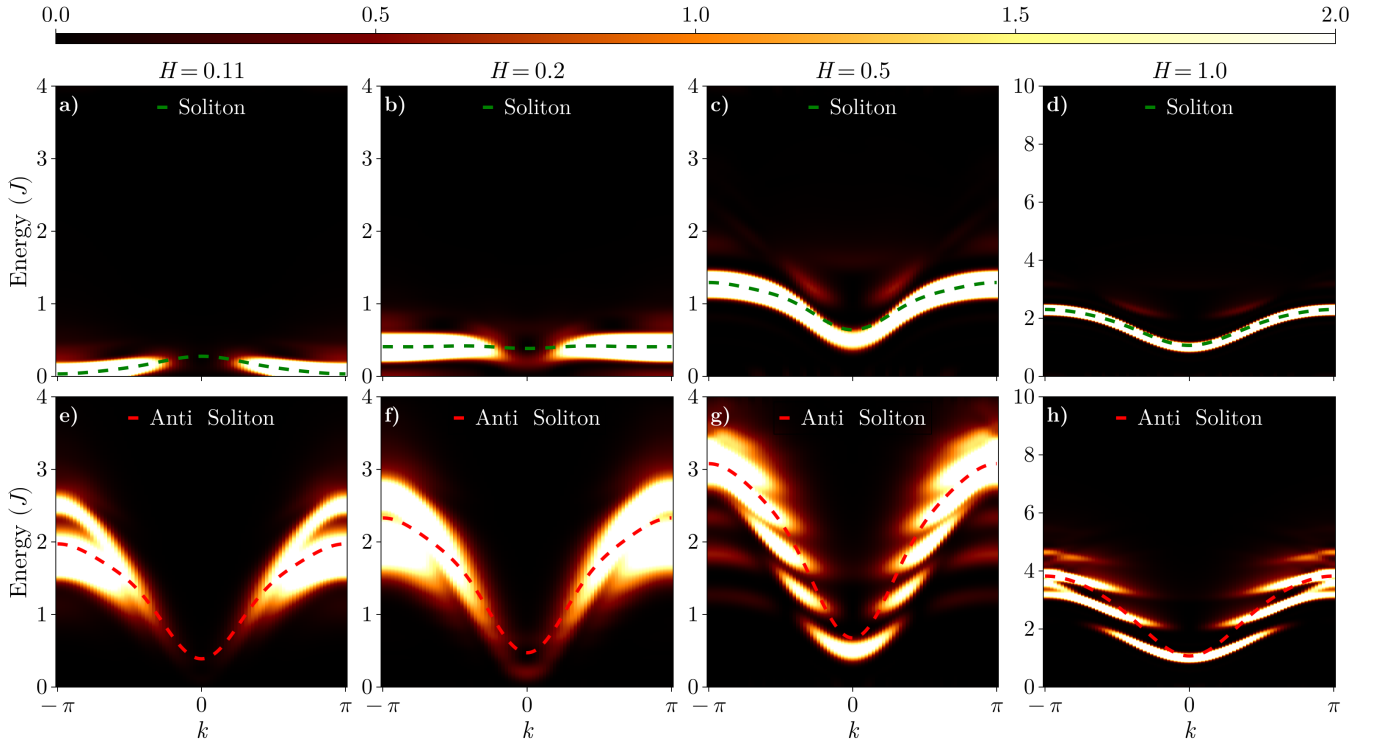


FIG. 11. Dynamical soliton–soliton (top) and antisoliton-antisoliton structure factor (bottom) for a chain of  $L = 84$  sites at (a,e)  $H = 0.11$ , (b,f)  $H = 0.2$ , (c,g)  $H = 0.5$ , and (d,h)  $H = 1.0$ . Note that the vertical axis scale changes for panels (d,h). The TEBD parameters are the same as in Fig. 10.

most energetically costly excitation, it tends to strongly overlap with, for instance, the magnon mode, thereby generating the enhanced spectral complexity observed. Far from being a drawback, such mode hybridization offers a pathway to experimentally “illuminate” solitonic excitations, as discussed in the following section.

## VI. EXPERIMENTAL SIGNATURES

In the previous section, we validated our effective low-energy theory against numerical calculations, showing that the sine-Gordon model provides an accurate description of the low-energy physics. To summarize: (i) the magnetization curve is well captured by the classical sine-Gordon prediction; (ii) the classical soliton solution offers a meaningful starting point for constructing a “quantum soliton” state; (iii) at the critical field, solitons soften and condense, giving rise to a Tomonaga-Luttinger liquid; and (iv) over a finite field range above saturation, solitons constitute the lowest-energy excitations.

Building on these results, we now identify experimental signatures of chiral solitons in real materials. The central finding is that magnon excitations, directly accessible through inelastic neutron scattering (INS), acquire a substantial hybridization with the soliton bands over a finite window of magnetic fields, making the solitons

observable in INS spectra. In addition, we show that the presence of soliton bands strongly modifies the field dependence of thermodynamic properties, most notably the specific heat.

### A. Magnon-soliton hybridization and inelastic neutron scattering

We begin by presenting the main results of this section, which will be examined in detail below. Fig. 12 shows the DSSF, as defined in Eq. (53), obtained from TEBD calculations for a chain with  $L = 84$  sites under magnetic fields  $H = 0.11, 0.2, 0.5$ , and  $1.0$ . As anticipated in previous sections, the results display pronounced deviations from the naive LSWT predictions. The spectrum reveals several rich and distinctive features, which we now analyze and relate to the effective theory of quantum solitons developed earlier.

To gain a deeper understanding of the features that emerge in the DSSF, it is useful to slightly shift our perspective. In the previous sections, we introduced the notion of quantum solitons semi-classically, i.e., as natural extensions of classical soliton solutions. A more quantum-mechanical viewpoint is to regard these solitons as linear combinations of single-magnon and multi-magnon bound states. The finite chirality is encoded in

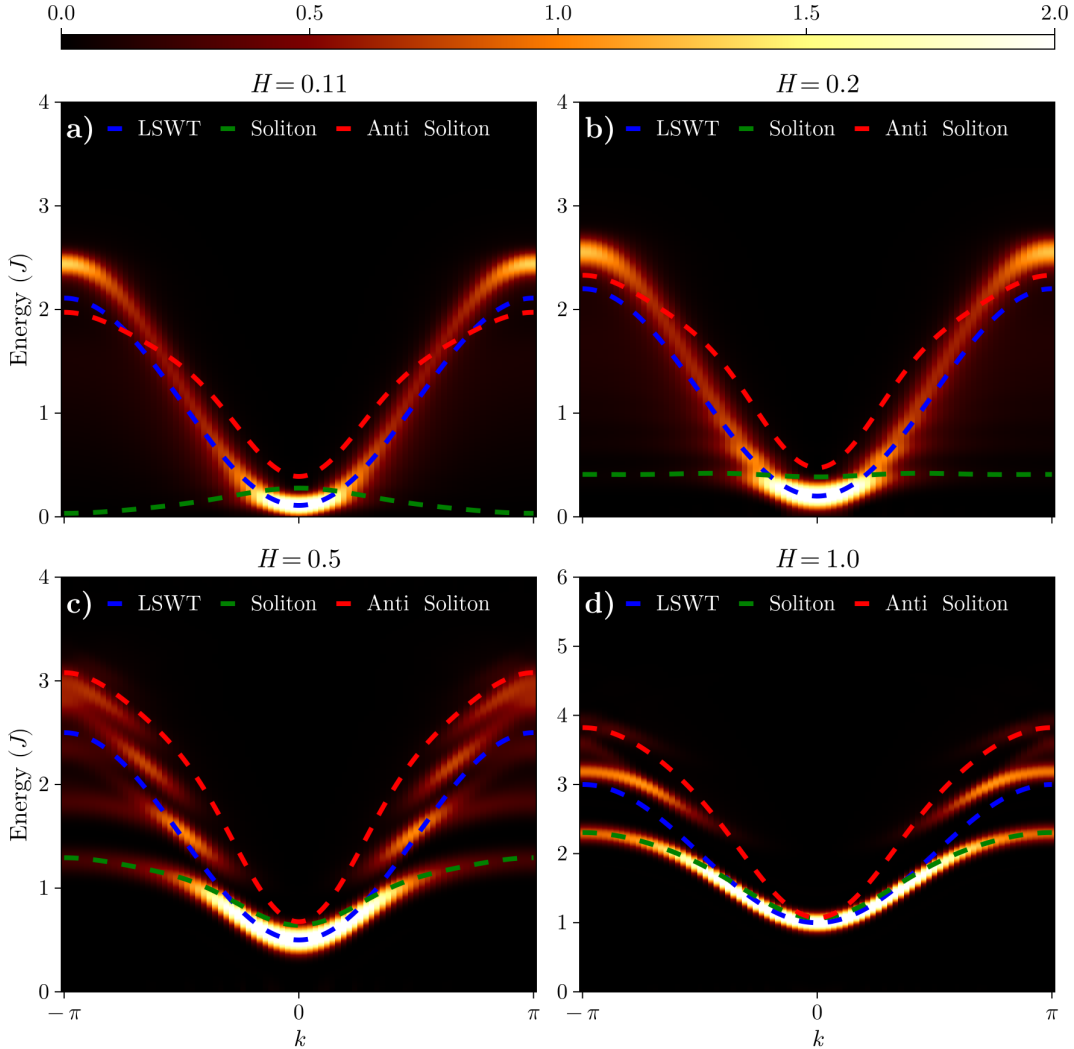


FIG. 12. DSSF for a chain of  $L = 84$  sites and (a)  $H = 0.11$ , (b)  $H = 0.2$ , (c)  $H = 0.5$ , (d)  $H = 1.0$ . The TEDB parameters are the same as those for Fig. 10. The hybridization between the magnon mode and the soliton mode is practically absent for  $H \approx H_c$  because magnons with  $k \approx 0$  are practically exact eigenstates. As expected, an incipient soliton magnon hybridization becomes apparent for  $H \approx 0.2$  because the two bands cross far enough from  $k = 0$ . In addition, we can also observe hybridization between the magnon band and the multi-soliton continuum because the level crossings occur even further away from  $k = 0$ . This behavior becomes more evident for  $H = 0.5$ , where the full soliton band becomes visible due to hybridization with the soliton band. For  $H = 1$  we can no longer distinguish the soliton and the magnon modes because the soliton size is of the order of the lattice space.

the coefficients of the linear combination.

Inelastic neutron scattering (INS) probes excitations with  $\Delta S^x = \pm 1, 0$ . The lack of U(1) symmetry in  $\hat{H}_S$  arises from the DM term, that mixes different particle-number (magnetization) sectors. In other words, the magnetization along the field direction is not a good quantum number for general eigenstates. The fully polarized ground state  $|0\rangle$  above the saturation field and the zero momentum single magnon state  $\hat{S}_{k=0}^z |0\rangle$  are exceptions to this rule [see Appendix B] because they are exact eigenstates with magnetizations  $L/2$  and  $L/2 - 1$ , respectively.

For sufficiently high magnetic fields the U(1) symmetry is approximately restored because the energy gap between different magnetization (particle number) sectors becomes much larger than the matrix elements of the DM term. In this regime, the excitations probed by INS correspond to single magnons across the Brillouin zone [see Fig. 10]. As the magnetic field is lowered, the situation changes qualitatively because of two key effects. First, while the multi-magnon bound states have a higher Zeeman energy cost—since they correspond to multiple flipped spins—they simultaneously gain energy through their mutual binding interactions. This binding energy

lowers their total excitation energy, causing the bound-state branches to shift downward in the spectrum. As a result, in an intermediate-field regime, the energies of single-magnon and multi-magnon bound-state excitations approach one another, enabling strong hybridization due to the DM interaction. This hybridization transfers spectral weight from the more intense single-magnon modes to the bound states, making the latter directly observable in the DSSF.

Fig. 12(d) illustrates this behavior at  $H = 1.0 \approx 10H_c$ . Two main bands are clearly visible, with the lower-energy branch showing excellent agreement with the soliton band derived in Sec. IV. At this field, the classical soliton size, estimated from the magnetization jump relative to the ground state, is  $\Delta M^x \approx 1.41$ , placing it between the one- and two-magnon bound-state sectors. Although referring to this excitation as a “soliton” is somewhat of an abuse of terminology, since its spatial extent becomes comparable to the lattice spacing, we retain the name to emphasize its continuous evolution into the true soliton mode as  $H$  approaches  $H_c$ .

A natural next step is to quantify the hybridization between these two branches. As shown in Appendix H, this analysis yields, within controlled approximations, the following band structure:

$$E(k) \approx \begin{cases} \epsilon_2(k) + \frac{D^2}{H} \sin^4(k/2), \\ \epsilon_1(k) - \frac{D^2}{H} \sin^4(k/2), \end{cases} \quad (56)$$

where  $\epsilon_1(k) = H + 2J \sin^2(k/2)$  and  $\epsilon_2(k) = 2H + J \sin^2(k/2)$ . As shown in Fig. 13, this simple description reproduces the high-energy band remarkably well, while slightly overestimating the energy of the low-energy branch for  $k > \pi/2$ .

The figure also shows that the high-energy magenta band corresponds to the lower edge of the two-soliton continuum (green dots), with its spectral intensity vanishing as it approaches the two-magnon continuum (blue dots). As discussed previously, at  $k = 0$  only the magnon excitation is visible in INS, since  $\hat{\tilde{S}}_{k=0}^z |0\rangle$  is an eigenstate.

The situation shown in Fig. 12(c), corresponding to  $H = 0.5 \approx 5H_c$ , is more intricate, and the excitation spectrum displays a noticeably richer structure. Nevertheless, the lower branch remains in excellent agreement with the soliton dispersion obtained from our effective theory. To elucidate the origin of the additional bands, we employ an approach analogous to that used for  $H = 1$ , but now we consider the hybridization among a larger set of states: the soliton, the antisoliton, the single-magnon excitation, and a composite state formed by a  $k = 0$  magnon together with a soliton of momentum  $k$ ,

$$|\alpha_k\rangle = \frac{\hat{\tilde{S}}_{k=0}^z \hat{T}_k^\dagger |0\rangle}{\sqrt{\langle 0 | \hat{\tilde{T}}_k (\hat{\tilde{S}}_{k=0}^z)^2 \hat{\tilde{T}}_k^\dagger | 0 \rangle}}, \quad (57)$$

which, together, span the low-energy subspace  $\mathcal{S}_0$ .

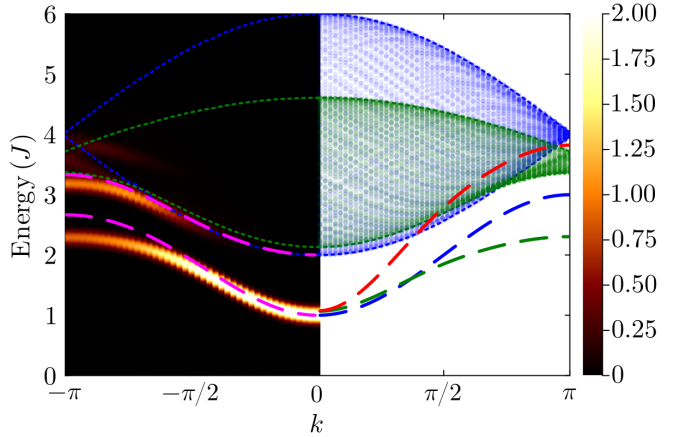


FIG. 13. Left: Dynamical spin structure factor showing the bands obtained via Eq. 56 (magenta dashed line). Right: Two-magnon continuum (blue dots) and two-soliton continuum (green dots), together with the magnon bands (blue dashed), soliton bands (green dashed), and antisoliton band (red dashed). These calculations correspond to  $H = 1$ .

The next step is to project the Hamiltonian onto the subspace spanned by these states in order to compute the resulting hybridized band structure. A crucial technical point is that the original states are not mutually orthogonal. To address this non-orthogonality while still retaining the dominant physical character of each state, we construct an orthonormal basis using *Löwdin orthogonalization* [38, 39], a symmetric procedure that transforms a set of non-orthogonal vectors  $\{|\phi_j\rangle\}$  into an orthonormal basis  $\{|\psi_j\rangle\}$  while preserving, as closely as possible, the geometric structure of the original subspace. This allows us to diagonalize the Hamiltonian in a well-defined orthonormal basis and to unambiguously identify the physical origin of the different spectral branches observed in the DSSF.

Specifically, given the overlap matrix,

$$S_{jj'} = \langle \phi_j | \phi_{j'} \rangle, \quad (58)$$

the Löwdin orthogonalized states are defined as:

$$|\psi_j\rangle = \sum_l S_{jl}^{-1/2} |\phi_l\rangle. \quad (59)$$

This construction ensures  $\langle \psi_j | \psi_{j'} \rangle = \delta_{jj'}$  while keeping the new basis, in the least-squares sense, as close as possible to the original set of vectors.

In this new basis  $\{|\psi_j\rangle\}$ , which consists of linear combinations of the states introduced above (with the momentum dependence suppressed for notational simplicity), we compute the matrix elements of the Hamiltonian projected onto the subspace  $\mathcal{S}_0$ :

$$h_{jj'}^{\text{multi}}(k) = \langle \psi_j | \hat{H}_S | \psi_{j'} \rangle - E_0 \delta_{jj'}. \quad (60)$$

Diagonalizing the resulting matrix yields the hybridized modes. The resulting bands are shown in Fig. 14.

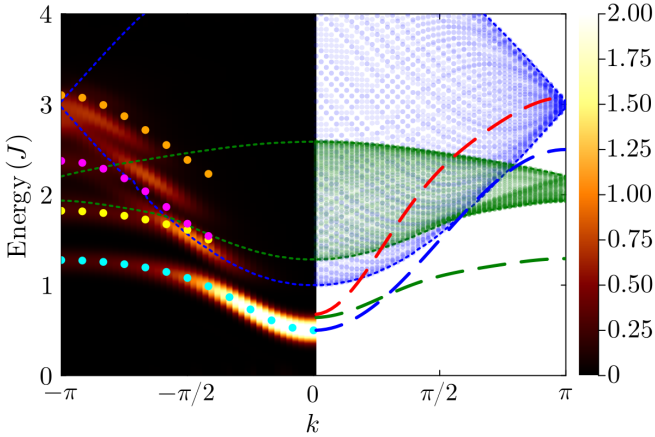


FIG. 14. Left: Dynamical spin structure factor showing the bands obtained via the hybridization procedure described in the text (cyan, yellow, magenta, and orange dots). Right: Two-magnon continuum (blue dots) and two-soliton continuum (green dots), together with the magnon bands (blue dashed), soliton bands (green dashed), and antisoliton band (red dashed). Calculations correspond to  $H = 0.5$ .

As shown on the left side of Fig. 14, the main dispersive bands are accurately reproduced using the described procedure, retaining strong coherence up to their entry into the two-magnon and two-soliton continua (right side of Fig. 14). More importantly, the fact that all four excitations are clearly “visible” in INS demonstrates that this field range represents a “sweet spot” where both the soliton and antisoliton dispersions become experimentally accessible.

As the field approaches the critical value  $H_c$ , the lowest-energy excited state evolves into a linear combination of several bound states, which can now be identified more precisely with the semiclassical soliton. The soliton gap gradually closes and this mode condenses, giving rise to the Tomonaga–Luttinger liquid phase discussed earlier. From a spectroscopic standpoint, the overlap between the soliton and the single-magnon excitation becomes very small near  $H_c$ , rendering the soliton mode almost invisible to INS measurements.

A careful inspection of Figs. 12(a) and 12(b) nevertheless reveals distinct solitonic signatures in the excitation spectrum. Momentum cuts, shown in Fig. 15, highlight these features and provide a clearer view of the solitonic contributions.

As a final verification of the nature of the excitations, we compute the fidelity between the exact eigenstates and the variational soliton, antisoliton, and magnon states, defined as:

$$\mathcal{F}_m = \left| \langle n | \hat{\tilde{S}}_k^z | 0 \rangle \right|^2, \quad \mathcal{F}_\tau = \left| \langle n | \hat{T}_{k\tau}^\dagger | 0 \rangle \right|^2, \quad (61)$$

where  $|n\rangle$  denotes the exact eigenstates obtained from exact diagonalization of a system with  $L = 12$  sites.

In Fig. 16, we present the results for the same field values considered previously, evaluated at  $k = \pi$ , together

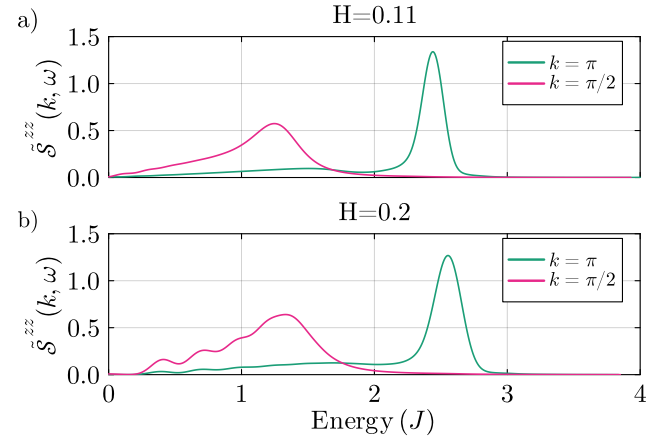


FIG. 15. Constant momentum cuts of the dynamical spin structure factor  $\tilde{\mathcal{S}}^{zz}(k, \omega)$  taken at  $k = \pi$  and  $k = \pi/2$  for external fields  $H = 0.11$  (a) and  $H = 0.2$  (b).

with the longitudinal magnetization  $\Delta M_{\text{exc}}^x$  of the eigenstates that exhibit at least one high-fidelity match. Notably, the lowest-energy excitation shows a pronounced solitonic character (green dot) [Figs. 16(a)–(d)], with a fidelity  $\mathcal{F}_s \approx 0.95$ . Its longitudinal magnetization [Figs. 16(e)–(h)] also agrees closely with the value expected for the soliton (green star).

The situation becomes more intricate for higher excitations. As discussed above, the magnon and antisoliton strongly hybridize with the two-soliton continuum, making their character less well defined. This is reflected in the mismatch of their longitudinal magnetizations [Figs. 16(e)–(h), red and blue stars]. Even in this mixed regime, some robust features persist: in Figs. 16(a)–(b) we observe clear crossovers between magnonic and antisolitonic excitations, while in Figs. 16(c)–(d) the higher-energy modes are predominantly antisolitonic. For  $H = 0.5$ , the intermediate-energy bands highlighted in yellow and magenta in Fig. 14 are chiefly magnonic, whereas the cyan (lowest-energy) and orange (highest-energy) branches are primarily solitonic and antisolitonic, respectively [see Fig. 16(c)].

As the field increases further, the soliton character remains robust in the lowest excitation, but the mode gradually acquires a significant magnon component (blue dot), reflecting the continuous evolution of the soliton into a magnon. This crossover is what ultimately enables inelastic neutron scattering to detect the soliton mode. Throughout this regime, the longitudinal magnetization of the first exact excitation continues to match closely the value expected for the soliton.

## B. Thermodynamic properties

No less remarkable are the thermodynamic consequences of the emergence of solitons as low-energy excitations of the system. As discussed throughout this

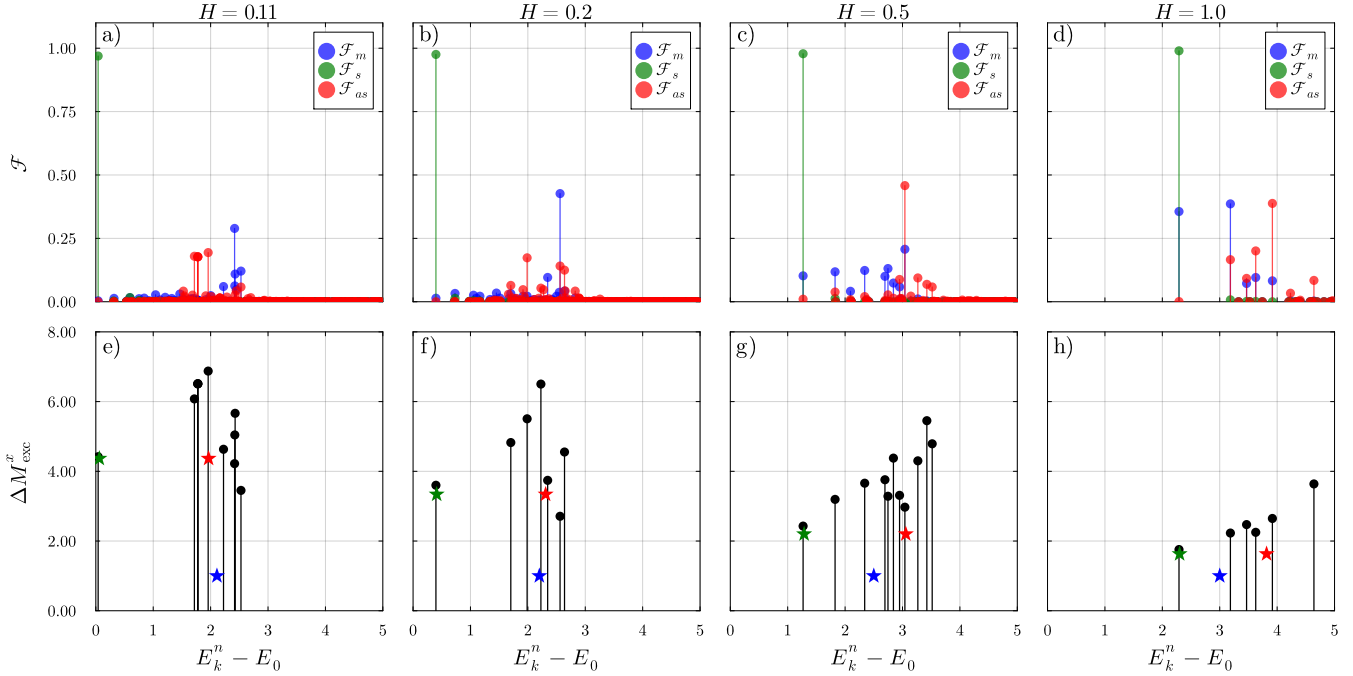


FIG. 16. (a–d) Character fidelity, as defined in Eq. 61, and (e–h) magnetization difference  $\Delta M_{exc}^x$  of the first excitations at momentum  $k = \pi$  for different magnetic fields. The stars in the bottom panels indicate the mean energy and magnetization values corresponding to the magnon (blue), soliton (green), and antisoliton (red) excitations.

work, for fields slightly above the saturation value, solitons constitute the lowest-energy excitations and exhibit a dispersive spectrum. Owing to the relatively flat soliton dispersion in this field range, a Schottky-like anomaly is expected to appear in the specific heat,

$$C_v = \frac{1}{L} \frac{dU}{dT}, \quad (62)$$

where  $U$  denotes the internal energy. This low-temperature feature should be followed by a broader magnon-induced contribution at higher energies. At larger fields, the Schottky anomaly is expected to merge with the magnon contribution, resulting in a single broad peak in the specific heat.

Furthermore, because creating a soliton involves a substantial change in the total magnetization, a pronounced response is also expected in the temperature derivative of the magnetization. At the critical field  $H = H_c$ , the free-fermion fixed point implies a characteristic divergence  $L^{-1}dM^x/dT \propto 1/\sqrt{T}$ . To test this expectation, we performed exact diagonalization calculations for a system with  $L = 12$  sites, and the resulting behavior is shown in Fig. 17.

These observations, together with the magnetization curve shown in Fig. 8, provide clear and accessible signatures of solitonic excitations through relatively simple experimental measurements. They thus offer a practical strategy for identifying promising candidate materials for INS studies, where the presence of these excitations can be unambiguously established using the analysis pre-

sented in the previous section.

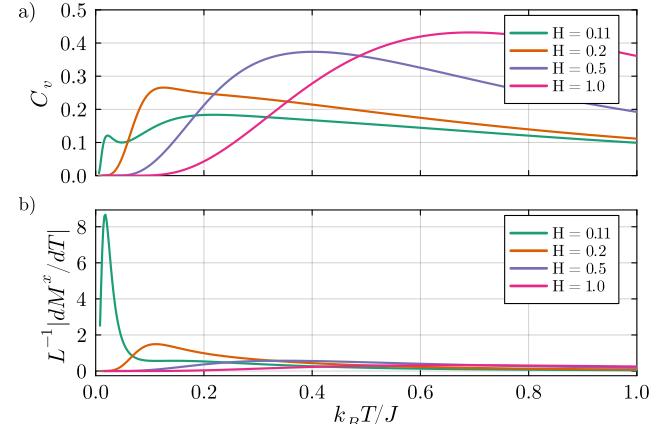


FIG. 17. Temperature dependence of the specific heat (a) and of the absolute value of the temperature derivative of the total magnetization along the field direction (b) for a system with  $L = 12$  sites under different external magnetic fields.

## VII. DISCUSSION

In this work, we employed a nonperturbative approach to capture the quantum effects of mesoscale spin- $\frac{1}{2}$  chiral solitons on a one-dimensional lattice. By “mesoscale,” we refer to solitons spanning several lattice spacings ( $\lesssim$

10), where quantum effects become sufficiently strong to generate dynamics beyond semiclassical descriptions.

We developed an effective theory in which chiral solitons are treated as hard-core bosonic quasiparticles within a coarse-grained picture. Quantum fluctuations were incorporated via a standard Wannierization procedure, yielding an orthonormal basis of single-particle states that may be interpreted as classical solitons dressed by tightly localized quantum fluctuations. Using this basis, we analytically computed the tunneling amplitudes between lattice sites and constructed a tight-binding Hamiltonian that captures the effective soliton dynamics. While the formulation was initially restricted to the single-soliton sector, it naturally extends to the dilute regime just below the saturation field.

The resulting lattice theory connects directly to the sine-Gordon-Thirring duality, bridging field-theoretical and lattice descriptions of solitonic excitations. Unlike in the Thirring model, the soliton and antisoliton bands on the lattice acquire different masses and dispersions, with the soliton band minimum shifting from  $k = 0$  to  $k = \pi$  below a characteristic field  $H_0 > H_c$ .

These features open a pathway for detecting chiral soliton excitations in one-dimensional quantum magnets. In particular, the quasi-flat soliton band at  $H = H_0$ , together with the magnon band, produces a characteristic double-peak structure in the specific heat for  $H \lesssim H_0$ , merging into a single broad feature for  $H > H_0$ . As the field increases and the soliton size decreases, mesoscale soliton modes acquire a finite single-magnon character, thereby enabling their direct observation via inelastic neutron scattering.

While several antiferromagnetic (AF) spin-chain materials with uniform Dzyaloshinskii–Moriya (DM) interactions are known—including  $\text{CsCoCl}_3$  [40],  $\text{Ba}_2\text{CuGe}_2\text{O}_7$  [41] (which is, however, quasi-two-dimensional [42]), and  $\text{K}_2\text{CuSO}_4\text{Br}_2$  [43]—their phase diagrams differ qualitatively from the ferromagnetic scenario discussed here. In AF systems, the fully polarized phase and the incommensurate soliton-lattice phase are separated by an intermediate commensurate canted phase [41], referred to as the  $N^y$  state in theoretical studies [44, 45]. This intermediate phase imposes distinct kinematic constraints and decay channels compared to the ferromagnetic case, where the soliton band may emerge below the continuum as a sharp, well-defined excitation. It would be interesting to investigate whether solitons could appear as high-energy excitations in the INS spectrum within the  $N^y$  phase (or possibly within the polarized state).

Although ferromagnetic insulators are comparatively less common, several notable examples of systems comprising ferromagnetic chains exist. Prototypical realizations include the  $S = \frac{3}{2}$  ferromagnet  $\text{CrNb}_3\text{S}_6$ , extensively studied in Ref. [46], and the  $S = 1$  compound  $\text{CsNiF}_3$  [47–49]. As well as the effective  $S = \frac{1}{2}$  chain systems such as  $\text{CoNb}_2\text{O}_6$  [50] and  $\text{CsCuCl}_3$  [51–53]. In the latter, the absence of inversion symmetry between

neighboring  $\text{Cu}^{2+}$  ions allows for a uniform DM interaction along the chain direction. However, the ratio of interchain to intrachain exchange is not sufficiently small to regard this material as strictly quasi-one-dimensional. Materials with reduced interchain coupling would provide natural platforms for realizing and exploring the solitonic behavior described in this work. Lastly, the  $S = \frac{1}{2}$  chiral compound  $\text{YbNi}_3\text{Al}_9$  has shown strong signatures of hosting solitonic physics, although an effective model has not yet been obtained [54, 55].

Turning to the extension of the present work to two-dimensional ( $D = 2+1$ ) systems, several studies have incorporated quantum fluctuations into baby-skyrmion excitations arising in two-dimensional generalizations of our Hamiltonian [32–34, 56–59]. In particular, Takashima *et al.* [34] and Haller *et al.* [32] employ approaches closely related to ours: they construct skyrmion creation operators and, in the latter case, incorporate quantum fluctuations through a variational framework. This strategy allows them to identify renormalizations of skyrmion parameters and even to propose the existence of a skyrmion-liquid phase.

A key challenge, however, is that—unlike the chiral-soliton physics discussed in this work—the field-induced transition between the skyrmion-crystal phase and the fully polarized state is strongly first order for the classical spin Hamiltonians known to host skyrmion crystals. This feature stands in sharp contrast to the one-dimensional case considered here, where the soliton density can be tuned continuously. As a result, one gains access to a dilute regime in which solitons move freely and appear as well-defined low-energy excitations above the fully polarized background.

A further obstacle is the substantially greater computational complexity of two-dimensional simulations. For example, DMRG calculations typically require cylindrical geometries, which break translational invariance along one direction and consequently pin and localize skyrmions, complicating the analysis of their intrinsic dynamics.

We hope that our detailed analysis of one-dimensional quantum solitons will motivate more theoretical and experimental studies of these unusual excitations.

## ACKNOWLEDGMENTS

The authors are grateful to Yusuke Kato for insightful discussions. We thank Kirill Povarov and Andrew Christianson for the discussion of the experimental situation. L.M.C. was supported by the U.S. Department of Energy, Office of Science, Basic Energy Sciences, Materials Science and Engineering Division. C.D.B. acknowledges support from the U.S. Department of Energy, Office of Science, Office of Basic Energy Sciences, under Award Number DE-SC0022311.

## Appendix A: Semiclassical derivation of the sine-Gordon Hamiltonian

The classical continuum limit of  $\hat{H}_S$  (Eq. (1)) is obtained by parameterizing the spin at site  $j$  as  $S_j = S(\sin \theta_j \cos \varphi_j, \sin \theta_j \sin \varphi_j, \cos \theta_j)$  and replacing lattice differences with spatial derivatives to obtain:

$$H = \int dx JS^2 a \left( \frac{1}{2} (\partial_x \theta)^2 + \frac{1}{2} \sin^2 \theta (\partial_x \varphi)^2 + q_0 \sin^2 \theta \partial_x \varphi - m^2 \sin \theta \cos \varphi \right), \quad (\text{A1})$$

where  $a$  is the lattice spacing,  $x = ja$  is the continuous coordinate,  $q_0 = D/(Ja)$ , and  $m^2 = H/(JSa^2)$ . It proves convenient to remove the linear derivative term by defining  $\tilde{\varphi} = \varphi - q_0 x$  so that,

$$H = \int dx JS^2 a \left( \frac{1}{2} (\partial_x \theta)^2 + \frac{1}{2} \sin^2 \theta (\partial_x \tilde{\varphi})^2 - \frac{1}{2} q_0^2 \sin^2 \theta - m^2 \sin \theta \cos(\tilde{\varphi} + q_0 x) \right). \quad (\text{A2})$$

Time dynamics of the continuous fields  $\theta, \tilde{\varphi}$  follow from the Landau-Lifshitz equations. An elegant way to incorporate them is via Euler-Lagrange equations of the associated Lagrangian, [12, 60]

$$L = \int dx \left( \frac{1}{g} (\cos \theta - 1) \dot{\tilde{\varphi}} - \mathcal{H} \right) \quad (\text{A3})$$

where  $\mathcal{H}$  is the Hamiltonian density (the integrand of Eq. (A2)) and the dot in the first, Berry phase term denotes time derivative  $\partial_t$ . Fields  $\theta$  and  $\tilde{\varphi}$  depend on  $x$  and  $t$ , and we abbreviated  $1/g = S/a$ .

An efficient way to get the result is to set  $\theta = \pi/2 + \tilde{\theta}$  in Eq. (A3) and expand the Lagrangian up to quadratic terms in  $\tilde{\theta}$ ,

$$L = \int dx \left( -\frac{1}{g} \dot{\tilde{\varphi}} - \frac{1}{g} \tilde{\theta} \dot{\tilde{\varphi}} - JS^2 a \left[ \frac{1}{2} q_0^2 \tilde{\theta}^2 + \frac{1}{2} (\partial_x \tilde{\theta})^2 + \frac{1}{2} (\partial_x \tilde{\varphi})^2 - m^2 \cos(\tilde{\varphi} + q_0 x) \right] \right), \quad (\text{A4})$$

For small  $|\partial_x \tilde{\theta}| \ll q_0 \tilde{\theta}$ , the second term in square brackets can be dropped as well [61].

The Lagrangian form in configuration space,  $L = L(\tilde{\varphi}, \dot{\tilde{\varphi}})$ , is obtained by integrating out  $\tilde{\theta}$ . Since the Lagrangian is quadratic in  $\tilde{\theta}$ , this is equivalent to replacing  $\tilde{\theta}$  with the solution of the equation of motion:

$$\frac{\delta L}{\delta \tilde{\theta}} = -\frac{1}{g} \dot{\tilde{\varphi}} - JS^2 a q_0^2 \tilde{\theta} = 0, \quad (\text{A5})$$

which gives,

$$\tilde{\theta}(x) = -\frac{1}{g JS^2 a} \frac{1}{q_0^2} \dot{\tilde{\varphi}}(x). \quad (\text{A6})$$

The resulting Lagrangian form in configuration space is:

$$L = \int dx \left( JS^2 a \left[ \frac{1}{2c^2} (\partial_t \tilde{\varphi})^2 - \frac{1}{2} (\partial_x \tilde{\varphi})^2 + m^2 \cos(\tilde{\varphi} + q_0 x) \right] - \frac{1}{g} \partial_t \tilde{\varphi} \right). \quad (\text{A7})$$

with  $c = g q_0 J S^2 a = g D S^2$ .

Going back to phase space, the sine-Gordon Hamiltonian can now be expressed in terms of the field  $\varphi$  and the conjugate momentum  $\tilde{\Pi} = (JS^2 a/c^2) \partial_t \tilde{\varphi} - 1/g$ :

$$\tilde{H}_{\text{sG}} = \int dx \mathcal{H}_{\text{sG}}, \quad (\text{A8})$$

where

$$\mathcal{H}_{\text{sG}} = \frac{cK}{2} (\tilde{\Pi} + \frac{1}{g})^2 + \frac{c}{2K} (\partial_x \tilde{\varphi})^2 - \frac{HS}{a} \cos[\tilde{\varphi} + q_0 x], \quad (\text{A9})$$

where  $K = g q_0$ , and we simplified the coefficient of the cosine term using the definition of  $m^2$ . Observe the persistence of a slightly unusual constant term  $1/g$  that originates from the linear time-derivative term in Eq. (A3).

Next, rescale  $\tilde{\Pi} = \Pi/\sqrt{4\pi}$ ,  $\tilde{\varphi} = \sqrt{4\pi}\varphi$ , and  $K = 4\pi\kappa$ , so that the commutation relation  $[\tilde{\varphi}(x), \tilde{\Pi}(x')] = [\varphi(x), \Pi(x')] = i\delta(x - x')$  is preserved. In addition, we undo the position-dependent shift of the field  $\varphi$ ,  $\varphi(x) \rightarrow \varphi(x) - q_0 x/\sqrt{4\pi}$ , to obtain,

$$\mathcal{H}_{\text{sG}} = \frac{c\kappa}{2} (\Pi + \frac{\sqrt{4\pi}}{g})^2 + \frac{c}{2\kappa} (\partial_x \varphi)^2 - \frac{cq_0}{\sqrt{4\pi}\kappa} \partial_x \varphi - \frac{HS}{a} \cos[\sqrt{4\pi}\varphi], \quad (\text{A10})$$

We observe that momentum  $\Pi$  appears in a sum

$$\Pi + \frac{\sqrt{4\pi}}{g} = \Pi + \Pi_0, \quad (\text{A11})$$

with the “offset” momentum is  $\Pi_0 = \frac{\sqrt{4\pi}S}{a}$ .

A remarkable discovery by Coleman [13] and Mandelstam [14], and, independently, by Luther and Emery [28], is that Eq. (A11) can be exactly mapped to the Thirring model of massive Dirac fermions. The mapping is based on the observation that the exponential operator:

$$O(x) = e^{i\zeta \int_{-\infty}^x dx' \Pi(x')} \quad (\text{A12})$$

creates a soliton centered at  $x$ . This is proven with the help of the identity  $[A, e^B] = Ce^B$  that holds for any two operators  $A, B$  such that their commutator  $C = [A, B]$  commutes with both of them,  $[C, A] = [C, B] = 0$ .

The identity,

$$[\varphi(y), O(x)] = i \frac{\delta O(x)}{\delta \Pi(y)} = -\zeta \Theta(x - y) O(x) \quad (\text{A13})$$

means that the action of  $O(x)$  on an eigenstate  $|\varphi\rangle$  of the operator  $\hat{\varphi}$ , changes it to the state  $|\varphi'\rangle$  with the eigenvalue  $\varphi(y) - \zeta \Theta(x - y)$ . That is,

$$\varphi(y) \mapsto \begin{cases} \varphi(y) - \zeta, & y < x, \\ \varphi(y), & y > x. \end{cases}$$

In other words,  $O(x)$  creates a kink of height  $\zeta$  at position  $x$  in the field  $\varphi(y)$ . To describe solitons in Eq. (A11), we need to take  $\zeta = 2\pi/\sqrt{4\pi} = \sqrt{\pi}$ .

From here on, we make use of the powerful bosonization technique, which is described in vast detail in numerous reviews and textbooks. We chose to follow [25]. Introduce right- and left-moving fermions, describing propagating solitons, via:

$$\begin{aligned}\psi_+(x) &= \frac{1}{\sqrt{2\pi\alpha}} e^{i\sqrt{4\pi}\Phi_+(x)}, \\ \psi_-(x) &= \frac{i}{\sqrt{2\pi\alpha}} e^{-i\sqrt{4\pi}\Phi_-(x)},\end{aligned}\quad (\text{A14})$$

where the additional factor of  $i$  in  $\psi_-(x)$  is for future convenience. The chiral bosons are defined by:

$$\Phi_{\pm}(x) = \frac{1}{2} \left[ \varphi(x) \mp \int_{-\infty}^x dx' \Pi(x') \right] \quad (\text{A15})$$

Equations Eq. (A14) and Eq. (A15) show that  $e^{-i\sqrt{\pi} \int^x dx' \Pi(x')}$  is exactly the soliton operator, while the factors  $e^{\pm i\sqrt{\pi}\varphi(x)}$  are needed to enforce the Fermi statistics of the  $\psi_{\pm}$  fields [14].

Given that in our formulation momentum  $\Pi$  always appears together with  $\Pi_0$ , Eq. (A11), we can now shift it  $\Pi \rightarrow \Pi - \Pi_0$  to remove the offset. This changes Eq. (A15) by  $\Phi_{\pm} \rightarrow \Phi_{\pm} \mp \sqrt{\pi}S(x-L)/a$  where  $L \rightarrow -\infty$  is the (constant) contribution from the lower integration limit. Correspondingly, fermion operators  $\psi_{\pm}$  in Eq. (A14) change as

$$\psi_{\pm}(x) \rightarrow \psi_{\pm}(x) e^{-i\frac{2\pi S}{a}x} \quad (\text{A16})$$

(Since  $L/a$  is an integer, the phase factor  $e^{2\pi SL/a} = \pm 1$  can always be removed by a unitary transformation.) Equation Eq. (A16) signifies the shift of the soliton momentum by  $p_0 = 2\pi S/a$  relative to the origin. For the *integer* spin  $S$ , the shift is immaterial since then  $p_0$  is a multiple of the reciprocal lattice momentum. However, in the case of *half-integer* spin  $S$ , the shift  $p_0 = \pi/a$  actually describes the soliton that carries that Berry momentum  $p_0 = \pi/a$ .

We therefore conclude that chiral solitons are distinguished by a nontrivial quantum number, namely the momentum  $p_0$ . In the integer- $S$  chain the soliton momentum is zero,  $p_0 = 0$ , while in the half-integer- $S$  chain it is given by  $p_0 = \pi/a$ , the Brillouin zone boundary value. This effect is topological; it originates from the Berry phase in Eq. (A3). This unusual finding agrees with the earlier semiclassical studies by [29, 30].

Subsequent manipulations involve only the *slow*  $\psi_{\pm}(x)$  fields in the right-hand-side of Eq. (A16). This means, in particular, that in equations Eq. (A17) below, the *fast* oscillating factors  $e^{\pm ip_0 x}$  are not present at all. This is in complete similarity to the standard bosonization procedure when the fast-oscillating exponentials  $e^{\pm ik_F x}$  with Fermi-momenta  $\pm k_F$  are separated from the slow field  $\psi_{\pm}(x)$  describing right- and left-moving fermions which are bosonized according to the standard rules [25, 31].

Lengthy, but straightforward calculations [25] lead to the following set of bosonization identities,

$$\begin{aligned}\psi_+^\dagger(x)\psi_-(x) + \text{h.c.} &= \frac{1}{\pi\alpha} \cos[\sqrt{4\pi}\varphi(x)], \\ :\psi_+^\dagger(x)\psi_+(x) &:= \frac{1}{\sqrt{\pi}} \partial_x \Phi_+(x), \\ :\psi_-^\dagger(x)\psi_-(x) &:= \frac{1}{\sqrt{\pi}} \partial_x \Phi_-(x), \\ :\psi_+^\dagger(x)(-i\partial_x)\psi_+(x) &:= (\partial_x \Phi_+(x))^2, \\ :\psi_-^\dagger(x)(i\partial_x)\psi_-(x) &:= (\partial_x \Phi_-(x))^2.\end{aligned}\quad (\text{A17})$$

Dot columns signify normal ordering. These identities allow us to rewrite Eq. (A11) as the massive Thirring model of interacting fermions  $\psi_{\pm}$ ,

$$\begin{aligned}\mathcal{H}_{\text{mT}} &= \frac{c}{2} \left( \kappa + \frac{1}{\kappa} \right) [\psi_+^\dagger(x)(-i\partial_x)\psi_+(x) + \psi_-^\dagger(x)(i\partial_x)\psi_-(x)] \\ &+ \pi c \left( \kappa - \frac{1}{\kappa} \right) \psi_+^\dagger(x)\psi_+(x)\psi_-^\dagger(x)\psi_-(x) \\ &- \frac{cq_0}{2\kappa} [\psi_+^\dagger(x)\psi_+(x) + \psi_-^\dagger(x)\psi_-(x)] \\ &- \lambda [\psi_+^\dagger(x)\psi_-(x) + \psi_-^\dagger(x)\psi_+(x)]\end{aligned}\quad (\text{A18})$$

and  $\lambda = \pi HS\alpha/a$ . The first line represents the kinetic energy of Dirac fermions, while the second describes their interaction; notice that it vanishes for the special value of  $\kappa = 1$ . The third line shows that incommensuration  $q_0$  plays the role of the fermion chemical potential, while the nonlinear cosine potential now describes backscattering of  $\psi_{\pm}$  fermions (the last line). In the field theory language,  $\lambda$  is the mass term, responsible for the gap in the fermion spectrum.

It is worth noting again once that Eq. (A18) are written in terms of the slow  $\psi_{\pm}(x)$  field that do not contain  $e^{\pm ip_0 x}$  factors.

The essential physics of Eq. (A18) is understood by analyzing the non-interacting,  $\kappa = 1$ , (Luther-Emery) point [31].  $\mathcal{H}_{\text{mT}}(\kappa = 1)$  is diagonalized by:

$$\begin{pmatrix} \psi_+(k) \\ \psi_-(k) \end{pmatrix} = \begin{pmatrix} \alpha_k & \beta_k \\ -\beta_k & \alpha_k \end{pmatrix} \begin{pmatrix} u_k \\ d_k \end{pmatrix} \quad (\text{A19})$$

where

$$\begin{aligned}\alpha_k &= \frac{1}{\sqrt{2}} \left( 1 + \frac{c|k|}{\sqrt{c^2 k^2 + \lambda^2}} \right)^{1/2}, \\ \beta_k &= \frac{1}{\sqrt{2}} \left( 1 - \frac{c|k|}{\sqrt{c^2 k^2 + \lambda^2}} \right)^{1/2}.\end{aligned}\quad (\text{A20})$$

Note again that in accordance with our discussion above,  $k$  is measured from  $p_0$ . The  $u_k(d_k)$  fermions describe upper (lower) bands with dispersion  $(+/-)\epsilon_k - cq_0/2$ ,  $\epsilon_k = \sqrt{\lambda^2 + c^2 k^2}$ , representing solitons and antisolitons. As long as the chemical potential  $cq_0/2$  is inside the band gap,  $q_0 < q_c = 2\lambda/c$ , the lower band is completely full and the upper one is completely empty. The density of

solitons and antisolitons is zero. This is the commensurate vacuum, or high-field, state with  $\langle \partial_x \varphi \rangle = 0$ .

To describe soliton and antisoliton excitations on equal footing, it is convenient to make a particle-hole transformation for the occupied states:  $d_k \rightarrow h_{-k}^\dagger$ . The transformed Hamiltonian reads,

$$H_{\text{mT}}(\kappa = 1) = \sum_k \sqrt{c^2 k^2 + \lambda^2} (u_k^\dagger u_k + h_k^\dagger h_k) - \frac{cq_0}{2} (u_k^\dagger u_k - h_k^\dagger h_k) \quad (\text{A21})$$

Now,  $u_k(h_k)$  describes excitations, which are solitons (antisolitons), respectively.

Once the DM interaction becomes strong enough, or the magnetic field is reduced below the critical value,  $|q_0| > q_c$ , solitons enter the system. Positive  $q_0$  induces solitons, while  $q_0 < 0$  brings in antisolitons. The band structure Eq. (A21) is illustrated in Fig. 4(a).

Let us choose  $q_0 > 0$  for concreteness. The fermion density  $\rho = k_F/\pi$  determines the Fermi momentum  $k_F = \sqrt{q_0^2 - q_c^2}/2$ . According to Eq. (A17), the fermion density  $\rho = \langle \psi_+^\dagger(x) \psi_+(x) + \psi_-^\dagger(x) \psi_-(x) \rangle$  is directly proportional to  $\partial_x \varphi$ ,  $\langle \partial_x \varphi \rangle = \sqrt{\pi \rho}$ . This means that  $\langle \partial_x \varphi \rangle = \sqrt{(q_0^2 - q_c^2)/(4\pi)} \sim \sqrt{q_0 - q_c}$ . The state with the finite soliton density is the critical Luttinger liquid state of soliton liquid. Classically, this is the soliton lattice state described in Section II. Qualitative features of the described commensurate-incommensurate transition from the vacuum to the Luttinger liquid state persist for all values of  $\kappa$  [31].

## Appendix B: Exact eigenstates

Let us show that the fully polarized state along the  $\hat{x}$ -direction is an eigenstate of Hamiltonian Eq. (1). The proof for the Heisenberg term is straightforward, as this term is SU(2) invariant; therefore, any fully polarized state is an eigenstate. Similarly, the Zeeman term is trivially satisfied.

We now focus on the Dzyaloshinskii-Moriya (DM) part of the Hamiltonian, which, when rewritten in terms of ladder operators, takes the form:

$$\hat{H}_{\text{DM}} = -\frac{D}{2i} \sum_{l=1}^L \hat{h}_{l,l+1}, \quad (\text{B1})$$

with,

$$\hat{h}_{j,j+1} = \hat{S}_j^- \hat{S}_{j+1}^+ - \hat{S}_j^+ \hat{S}_{j+1}^-. \quad (\text{B2})$$

The fully polarized state is given by:  $|\Rightarrow\rangle = \frac{1}{2^{L/2}} \bigotimes_{l=1}^L [|\uparrow\rangle_l + |\downarrow\rangle_l]$  and the local action of  $\hat{h}_{l,l+1}$  on this state is:

$$\hat{h}_{l,l+1} [|\uparrow\rangle_l + |\downarrow\rangle_l] \otimes [|\uparrow\rangle_{l+1} + |\downarrow\rangle_{l+1}] = [|\downarrow\rangle_l |\uparrow\rangle_{l+1} - |\uparrow\rangle_l |\downarrow\rangle_{l+1}] \quad (\text{B3})$$

This implies that,

$$\begin{aligned} \hat{H}_{\text{DM}} |\Rightarrow\rangle &\propto \sum_{l=1}^L \left| \dots, [\downarrow_l \uparrow_{l+1} - \uparrow_l \downarrow_{l+1}], \dots \right\rangle \\ &\propto \sum_{l=1}^L \left| \dots, \downarrow_l \uparrow_{l+1}, \dots \right\rangle - \left| \dots, \uparrow_l \downarrow_{l+1}, \dots \right\rangle \end{aligned} \quad (\text{B4})$$

Now observe that the second term of the pair for index  $l$  is  $-|\dots \uparrow_l \downarrow_{l+1} \dots\rangle$ , which also is exactly the same as the first term of the pair with index  $l-1$ . That is, every basis configuration of the form  $|\dots \uparrow_l \downarrow_{l+1} \dots\rangle$  appears twice in the sum: once with a (+) sign coming from  $\hat{h}_{l,l+1}$ , and once with a (-) sign coming from  $\hat{h}_{l-1,l}$ . Therefore, the contributions cancel pairwise, and the complete sum vanishes, indicating that  $|\Rightarrow\rangle$  is an eigenstate of the DM part of the Hamiltonian with null eigenvalue. Finally, we have

$$\frac{1}{L} \hat{H}_S |\Rightarrow\rangle = -\left(\frac{J}{4} + \frac{H}{2}\right) |\Rightarrow\rangle. \quad (\text{B5})$$

Now we can also show that  $\hat{S}^z(k=0) |\Rightarrow\rangle$  is an eigenstate of  $\hat{H}_S$ . Indeed,

$$\hat{S}^z(k=0) = \frac{1}{\sqrt{L}} \sum_l \hat{S}_l^z = \frac{\hat{S}_{\text{tot}}^z}{\sqrt{L}}, \quad (\text{B6})$$

which is proportional to the total  $z$ -component of the magnetization. From the SU(2) invariance of the Heisenberg term, we have:

$$[\hat{H}_J, \hat{S}_{\text{tot}}^z] = 0,$$

and by the U(1) invariance around the  $z$ -axis of the DM term,

$$[\hat{H}_{\text{DM}}, \hat{S}_{\text{tot}}^z] = 0.$$

Thus,  $\hat{S}^z(k=0)$  acting on any eigenstate of  $\hat{H}_J + \hat{H}_{\text{DM}}$  also yields an eigenstate.

For the Zeeman contribution,

$$-H \sum_j \hat{S}_j^x = -H \hat{S}_{\text{tot}}^x,$$

the commutator gives

$$[\sqrt{L} \hat{S}^z(k=0), -H \hat{S}_{\text{tot}}^x] = -iH\sqrt{L} \hat{S}_{\text{tot}}^y. \quad (\text{B7})$$

Therefore,

$$\hat{S}_{\text{tot}}^x \hat{S}^z(k=0) |\Rightarrow\rangle = \left( \hat{S}^z(k=0) \hat{S}_{\text{tot}}^x - i \hat{S}_{\text{tot}}^y \right) |\Rightarrow\rangle. \quad (\text{B8})$$

From the first term on the r.h.s. we find,

$$\hat{S}^z(k=0) \hat{S}_{\text{tot}}^x |\Rightarrow\rangle = \frac{L}{2} \hat{S}^z(k=0) |\Rightarrow\rangle.$$

To compute the action of  $\hat{S}_{\text{tot}}^y$ , note that

$$\begin{aligned} i\hat{S}_l^y \frac{1}{\sqrt{2}}(|\uparrow\rangle_l + |\downarrow\rangle_l) &= \frac{1}{2\sqrt{2}}(|\uparrow\rangle_l - |\downarrow\rangle_l) \\ &= \hat{S}_l^z \frac{1}{\sqrt{2}}(|\uparrow\rangle_l + |\downarrow\rangle_l). \end{aligned} \quad (\text{B9})$$

By substituting this into Eq. (B8), we obtain,

$$\hat{S}_{\text{tot}}^x \hat{S}^z(k=0) |\Rightarrow\rangle = \left(\frac{L}{2} - 1\right) \hat{S}^z(k=0) |\Rightarrow\rangle, \quad (\text{B10})$$

which finally proves that  $\hat{S}^z(k=0) |\Rightarrow\rangle$  is an eigenvector

of  $\hat{H}_S$ ,

$$\hat{H}_S \hat{S}^z(k=0) |\Rightarrow\rangle = -\left(\frac{JL}{4} + H\left(\frac{L}{2} - 1\right)\right) \hat{S}^z(k=0) |\Rightarrow\rangle. \quad (\text{B11})$$

The energy difference between the fully polarized state and  $\hat{S}^z(k=0) |\Rightarrow\rangle$  is simply given by  $\Delta E = H$ , that is, merely the magnon gap in the fully-polarized phase.

### Appendix C: $\mathfrak{su}(2)$ algebra of soliton operators

This appendix presents the explicit calculations of the commutators involving the soliton and quantum-soliton operators. We begin with the former, evaluating

$$\begin{aligned} \hat{T}_{j\tau} \hat{T}_{j\tau}^\dagger &= \prod_{l \neq j} e^{i\varphi_\tau(l-j)\hat{S}_l^z} (\hat{S}_j^z - i\hat{S}_j^y)(\hat{S}_j^z + i\hat{S}_j^y) \prod_{l \neq j} e^{-i\varphi_\tau(l-j)\hat{S}_l^z} = \frac{1}{2} + i[\hat{S}_j^z, \hat{S}_j^y] = \frac{1}{2} + \hat{S}_j^x, \\ \hat{T}_{j\tau}^\dagger \hat{T}_{j\tau} &= (\hat{S}_j^z + i\hat{S}_j^y) \prod_{l \neq j} e^{-i\varphi_\tau(l-j)\hat{S}_l^z} \prod_{l \neq j} e^{i\varphi_\tau(l-j)\hat{S}_l^z} (\hat{S}_j^z - i\hat{S}_j^y) = \frac{1}{2} + i[\hat{S}_j^y, \hat{S}_j^z] = \frac{1}{2} - \hat{S}_j^x, \end{aligned} \quad (\text{C1})$$

which implies that the equal-site commutator is  $\hat{T}_{j\tau} \hat{T}_{j\tau}^\dagger - \hat{T}_{j\tau}^\dagger \hat{T}_{j\tau} = 2\hat{S}_j^x$ , while the anticommutator is  $\{\hat{T}_{j\tau}, \hat{T}_{j\tau}^\dagger\} = 1$ .

For different sites  $j' \neq j$  we have:

$$\begin{aligned} [\hat{T}_{j'\tau}, \hat{T}_{j\tau}^\dagger] &= (\hat{S}_{j'}^z + i\hat{S}_{j'}^y)(\hat{S}_j^z - i\hat{S}_j^y) \sum_{\sigma=\pm 1} \sigma e^{\sigma i\varphi_\tau(j'-j)\hat{S}_{j'\tau}^z} e^{\sigma i\varphi_\tau(j-j')\hat{S}_{j\tau}^z} \\ &= 2i(\hat{S}_j^z + i\hat{S}_j^y)(\hat{S}_{j'}^z - i\hat{S}_{j'}^y) \left[ f_\tau(j'-j)\hat{S}_j^z + f_\tau(j-j')\hat{S}_{j'}^z \right], \end{aligned} \quad (\text{C2})$$

where the function  $f_\tau(x) = \cos \varphi_\tau(x) \sin \varphi_\tau(-x)$  vanishes as  $x$  becomes much larger than the size of the chiral soliton [see Fig. 18]. Therefore, we can conclude that for all  $j$  and  $j'$ ,

$$[\hat{T}_{j'\tau}, \hat{T}_{j\tau}^\dagger] = 2\tilde{\delta}_{j'j\tau} \hat{S}_j^x \quad (\text{C3})$$

with  $\tilde{\delta}_{j'j\tau}$  denoting the coarse-grained version of the Kronecker delta. It is also straightforward to show that

$$\begin{aligned} [\hat{T}_{j\tau}^\dagger, \hat{S}_j^x] &= 2\hat{T}_{j\tau}^\dagger \\ [\hat{T}_{j'\tau}, \hat{S}_j^x] &= -2\hat{T}_{j'\tau} \end{aligned} \quad (\text{C4})$$

Based on this result, one can construct an approximate  $\mathfrak{su}(2)$  Lie algebra generated by  $\{\hat{T}_\tau^\dagger, \hat{T}_\tau, \hat{S}^x\}$ .

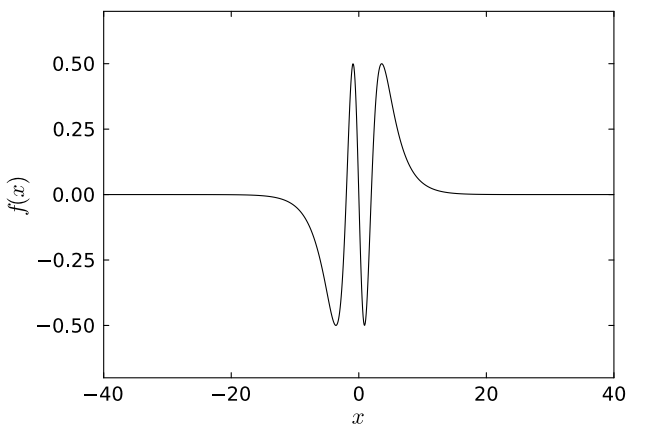


FIG. 18.  $f(x) = \cos \varphi(x) \sin \varphi(-x)$  as function of  $x = |l - j|$  for  $\tau = 1$ .

## Appendix D: Localization of the quantum soliton operator

We analyze the large-distance behavior of the expectation value  $\langle 0 | \hat{\mathfrak{T}}_{j\tau} \hat{T}_{j'\tau}^\dagger | 0 \rangle$ . Using the definition:

$$\hat{\mathfrak{T}}_{j\tau}^\dagger = \sum_p w_{j-p,\tau} \hat{T}_{p\tau}^\dagger, \quad \hat{\mathfrak{T}}_{j\tau} = \sum_p w_{j-p,\tau}^* \hat{T}_{p\tau}, \quad (\text{D1})$$

the expectation value can be expressed as:

$$\langle 0 | \hat{\mathfrak{T}}_{j\tau} \hat{T}_{j'\tau}^\dagger | 0 \rangle = \sum_p w_{j-p,\tau}^* O_{p,j'}, \quad (\text{D2})$$

where

$$O_{p,j'} = \langle 0 | \hat{T}_{p\tau} \hat{T}_{j'\tau}^\dagger | 0 \rangle \quad (\text{D3})$$

is given by Eq. (25). It is convenient to re-express the overlaps as:

$$O_{p,j'} = \sin^2 \frac{\varphi_\tau(j' - p)}{2} \prod_{l \neq p, j'} \cos \left[ \frac{\varphi_\tau(l - p) - \varphi_\tau(l - j')}{2} \right], \quad (\text{D4})$$

which follows from the relations  $\varphi_\tau(0) = \pi$  and  $\varphi_\tau(-x) = 2\pi - \varphi_\tau(x)$ . By applying periodic boundary conditions,  $x \mapsto \text{mod}(x + L/2, L) - L/2$ , both special factors ( $l = p$  and  $l = j'$ ) contribute positively because  $\cos[(\pi - \varphi_\tau(j' - p))/2] = \sin[\varphi_\tau(j' - p)/2]$ .

For large separations  $x = |j - j'|$  the soliton profile behaves as

$$\varphi(x) = 2\pi - 4e^{-Mx} + \mathcal{O}(e^{-3Mx}), \quad (\text{D5})$$

and therefore

$$\sin \frac{\varphi(x)}{2} = \sin(\pi - 2e^{-Mx}) \simeq 2e^{-Mx}, \quad (\text{D6})$$

which exhibits the expected exponential decay controlled by the mass scale  $M$ .

The product of cosines in Eq. (D4) remains of order unity, for sites  $h$  far from both centers  $p$  and  $j'$ ,  $\varphi(l - p) \approx \varphi(l - j')$  and  $\cos[(\varphi(l - p) - \varphi(l - j'))/2] \approx 1$ . The only deviations from unity arise from regions of width  $\sim 1/m$  near the kink centers, producing a finite,  $\mathcal{O}(1)$  prefactor  $C(m)$  that does not depend on the distance  $|l - p|$ .

Combining these results, we obtain for  $x \gg 1$ ,

$$O_{p,j'} \simeq \pm 4C(m) e^{-2m|j' - p|}. \quad (\text{D7})$$

Hence,  $O_{p,j'}$  decays exponentially with rate  $2p$ . Substituting Eq. (D7) into the definition of the full overlap yields:

$$\langle 0 | \hat{\mathfrak{T}}_{j\tau} \hat{T}_{j'\tau}^\dagger | 0 \rangle \simeq w_{j-j',\tau}^* + 4C(m) \sum_{p \neq j'} w_{j-p,\tau}^* e^{-2m|j' - p|}. \quad (\text{D8})$$

If the Wannier coefficients  $w_{j-p,\tau}$  are localized around  $p = j$ , the sum is dominated by  $p \simeq j$ , leading to the asymptotic behavior,

$$|\langle 0 | \hat{\mathfrak{T}}_{j\tau} \hat{T}_{j'\tau}^\dagger | 0 \rangle| \propto e^{-2m|j - j'|}. \quad (\text{D9})$$

In other words, the overlap between  $\hat{\mathfrak{T}}_{j\tau}^\dagger | 0 \rangle$  and  $\hat{T}_{j'\tau}^\dagger | 0 \rangle$  decays exponentially in the separation  $|j - j'|$ , with a correlation length  $\xi = 1/2m$ .

## Appendix E: Matrix elements for hoppings amplitudes

This Appendix presents the calculations for the matrix elements  $h_\tau(s)$  defined in the main text on Section IV D. The vacuum state corresponds to the fully polarized state along the  $x$ -direction, given by:

$$| 0 \rangle = \bigotimes_{l=1}^L \frac{1}{\sqrt{2}} \left[ |\uparrow\rangle_l + |\downarrow\rangle_l \right] \quad (\text{E1})$$

The action of the soliton (anti-soliton) operator centered at site  $j$  over the fully-polarized state is given by:

$$\left| \varphi_\tau^{(j)} \right\rangle \equiv \hat{T}_{j\tau}^\dagger | 0 \rangle = \bigotimes_{l=1}^L \frac{1}{\sqrt{2}} \left[ e^{-i\varphi_\tau(l-j)/2} |\uparrow\rangle_l + e^{i\varphi_\tau(l-j)/2} |\downarrow\rangle_l \right] \equiv \bigotimes_{l=1}^L |\mathbf{n}_l[\varphi_\tau(l-j)]\rangle, \quad (\text{E2})$$

where the last term defines the local coherent state  $|\mathbf{n}_l[\varphi_\tau(l-j)]\rangle$  at site  $l$ , associated with the soliton (anti-soliton) centered at site  $j$ . Note that the  $\mathbf{n}_l[\varphi_\tau(l-j)]$  unit vectors are perpendicular to the rotation  $z$ -axis and  $\varphi_\tau(l-j)$  is the corresponding azimuthal angle. The Hamiltonian of Eq. 1 can be decomposed into a sum of bilinear terms acting on pairs of neighboring sites  $n$  and  $n + 1$ , along with the Zeeman term that acts only on site  $n$ ,

$$\hat{H}_S = \sum_l \hat{h}_{l,l+1}^{(\text{Bi})} + \sum_l \hat{h}_l^{(Z)} \quad (\text{E3})$$

Following this, the matrix element of the Hamiltonian in the basis of the single soliton can be decomposed as:

$$\begin{aligned} \langle \varphi_\tau^{(j')} | H | \varphi_\tau^{(j)} \rangle &= \sum_l \langle \varphi_\tau^{(j')} | \hat{h}_{l,l+1}^{(\text{Bi})} | \varphi_\tau^{(j)} \rangle + \langle \varphi_\tau^{(j')} | \hat{h}_l^{(Z)} | \varphi_\tau^{(j)} \rangle \\ &= \sum_l \langle \mathbf{n}_{l+1}[\varphi_\tau(l+1-j')] | \langle \mathbf{n}_l[\varphi_\tau(l-j')] | \hat{h}_{l,l+1}^{(\text{Bi})} | \mathbf{n}_l[\varphi_\tau(l-j)] \rangle | \mathbf{n}_{l+1}[\varphi_\tau(l+1-j)] \rangle \prod_{p \neq l, l+1} \mathcal{O}_p^{j'j} \\ &\quad + \sum_l \langle \mathbf{n}_l[\varphi_\tau(l-j')] | \hat{h}_l^{(Z)} | \mathbf{n}_l[\varphi_\tau(l-j)] \rangle \prod_{p \neq l} \mathcal{O}_p^{j'j} \end{aligned} \quad (\text{E4})$$

with

$$\mathcal{O}_p^{j'j} \equiv \langle \mathbf{n}_p[\varphi_\tau(p-j')] | \mathbf{n}_p[\varphi_\tau(p-j)] \rangle = \cos \left[ \frac{\varphi_\tau(p-j') - \varphi_\tau(p-j)}{2} \right]. \quad (\text{E5})$$

We define,

$$F_{jj'}^\tau(x) \equiv \prod_{p \neq x} \mathcal{O}_p^{j'j} = \prod_{p \neq x} \cos \left[ \frac{\varphi_\tau(p-j') - \varphi_\tau(p-j)}{2} \right]. \quad (\text{E6})$$

Now we compute the matrix elements of the spin operators between two coherent states. Although only the expression for  $\hat{S}^x$  is needed, we include the remaining components for completeness:

$$\begin{aligned} \langle \mathbf{n}_l[\varphi_\tau(l-j')] | \hat{S}_n^x | \mathbf{n}_l[\varphi_\tau(l-j)] \rangle &= \frac{1}{2} \cos \left[ \frac{\varphi_\tau(l-j') + \varphi_\tau(l-j)}{2} \right] \\ \langle \mathbf{n}_l[\varphi_\tau(l-j')] | \hat{S}_n^y | \mathbf{n}_l[\varphi_\tau(l-j)] \rangle &= \frac{1}{2} \sin \left[ \frac{\varphi_\tau(l-j') + \varphi_\tau(l-j)}{2} \right] \\ \langle \mathbf{n}_l[\varphi_\tau(l-j')] | \hat{S}_n^z | \mathbf{n}_l[\varphi_\tau(l-j)] \rangle &= \frac{i}{2} \sin \left[ \frac{\varphi_\tau(l-j') - \varphi_\tau(l-j)}{2} \right] \end{aligned} \quad (\text{E7})$$

Using this result, the single-site matrix element for the Zeeman part of the Hamiltonian is given by,

$$\langle \mathbf{n}_l[\varphi_\tau(l-j')] | \hat{S}_n^x | \mathbf{n}_l[\varphi_\tau(l-j)] \rangle = -\frac{H}{2} \cos \left[ \frac{\varphi_\tau(l-j') + \varphi_\tau(l-j)}{2} \right] \quad (\text{E8})$$

The next step is to compute the matrix elements of the bilinear part of the Hamiltonian,

$$\langle \mathbf{n}_{l+1}[\varphi_\tau(l+1-j')] | \langle \mathbf{n}_l[\varphi_\tau(l-j')] | \hat{h}_{l,l+1}^{(\text{Bi})} | \mathbf{n}_l[\varphi_\tau(l-j)] \rangle | \mathbf{n}_{l+1}[\varphi_\tau(l+1-j)] \rangle \quad (\text{E9})$$

We note that the product state of two coherent states can be expressed as,

$$| \mathbf{n}_l[\varphi_\tau(l-j)] \rangle | \mathbf{n}_{l+1}[\varphi_\tau(l+1-j)] \rangle = \frac{1}{2} \begin{pmatrix} e^{-i\varphi_\tau(l-j)/2} e^{-i\varphi_\tau(l+1-j)/2} \\ e^{-i\varphi_\tau(l-j)/2} e^{i\varphi_\tau(l+1-j)/2} \\ e^{i\varphi_\tau(l-j)/2} e^{-i\varphi_\tau(l+1-j)/2} \\ e^{i\varphi_\tau(l-j)/2} e^{i\varphi_\tau(l+1-j)/2} \end{pmatrix}, \quad (\text{E10})$$

and the matrix representation of the two-site Heisenberg and DM Hamiltonian is given by

$$[\hat{\mathbf{S}}_l \cdot \hat{\mathbf{S}}_{l+1}] = \begin{pmatrix} 1/4 & 0 & 0 & 0 \\ 0 & -1/4 & 1/2 & 0 \\ 0 & 1/2 & -1/4 & 0 \\ 0 & 0 & 0 & 1/4 \end{pmatrix}, \quad [\hat{S}_l^x \hat{S}_{l+1}^y - \hat{S}_l^y \hat{S}_{l+1}^x] = \begin{pmatrix} 0 & 0 & 0 & 0 \\ 0 & 0 & i/2 & 0 \\ 0 & -i/2 & 0 & 0 \\ 0 & 0 & 0 & 0 \end{pmatrix}. \quad (\text{E11})$$

by evaluating the matrix elements and substituting them into Eq. (E4), we obtain:

$$\begin{aligned}
\langle \varphi_{\tau}^{(j')} | \hat{H}_S | \varphi_{\tau}^{(j)} \rangle = & -\frac{J}{8} \sum_n F_{j,j'}^{\tau}(l, l+1) \cos \left[ \frac{\varphi_{\tau}(l-j') + \varphi_{\tau}(l+1-j') - \varphi_{\tau}(l-j) - \varphi_{\tau}(l+1-j)}{2} \right] \\
& -\frac{J}{4} \sum_l F_{j,j'}^{\tau}(l, l+1) \cos \left[ \frac{\varphi_{\tau}(l-j') + \varphi_{\tau}(l-j) - \varphi_{\tau}(l+1-j') - \varphi_{\tau}(l+1-j)}{2} \right] \\
& +\frac{J}{8} \sum_l F_{j,j'}^{\tau}(l, l+1) \cos \left[ \frac{\varphi_{\tau}(l-j') - \varphi_{\tau}(l+1-j') - \varphi_{\tau}(l-j) + \varphi_{\tau}(l+1-j)}{2} \right] \\
& -\frac{D}{4} \sum_l F_{j,j'}^{\tau}(l, l+1) \sin \left[ \frac{\varphi_{\tau}(l+1-j') - \varphi_{\tau}(l-j') - \varphi_{\tau}(l-j) + \varphi_{\tau}(l+1-j)}{2} \right] \\
& -\frac{H}{2} \sum_l F_{j,j'}^{\tau}(l) \cos \left[ \frac{\varphi_{\tau}(l-j') + \varphi_{\tau}(l-j)}{2} \right].
\end{aligned} \tag{E12}$$

The hopping amplitudes can now be evaluated using Eq. 38 of the main text.

## Appendix F: Berry-phase origin of the integer/half-integer hopping sign alternation

This appendix shows that, within our lattice formulation, the minimum of the soliton band lies at  $k = \pi$  for half-integer spin chains and at  $k = 0$  for integer ones, in agreement with the continuum formulation discussed in Section III.

As shown in Appendix E, the soliton centered at site  $j$  is represented as a product of ( $S=1/2$ ) coherent spin states [see Eq. E2], a construction that extends straightforwardly to spin- $(S)$  coherent states.

In general, the phase of the overlap between two spin- $S$  coherent states at a given lattice site  $l$  is given exactly by the oriented solid angle on the Bloch sphere spanned by their corresponding spin directions and a chosen quantization axis. Keeping the fixed unit vector  $\hat{z}$ , parallel to the rotation axis of the skyrmion, as the quantization axis, let  $|\mathbf{n}_l\rangle$  and  $|\mathbf{n}'_l\rangle$  denote two coherent states satisfying

$$\langle \mathbf{n}_l | \hat{\mathbf{S}}_l | \mathbf{n}_l \rangle = S \mathbf{n}_l, \quad \langle \mathbf{n}'_l | \hat{\mathbf{S}}_l | \mathbf{n}'_l \rangle = S \mathbf{n}'_l,$$

where  $\hat{\mathbf{S}}_l = (\hat{S}_l^x, \hat{S}_l^y, \hat{S}_l^z)$  is the vector of spin- $S$  operators at site  $l$ . Note that this is just a generalization for arbitrary spin  $S$  of the  $S = 1/2$  coherent states introduced in the previous sections.

The argument of the overlap between a pair of coherent states is

$$\arg(\langle \mathbf{n}_l | \mathbf{n}'_l \rangle) = S \Omega(\hat{z}, \mathbf{n}_l, \mathbf{n}'_l) \pmod{2\pi}, \tag{F1}$$

where  $\Omega(\hat{z}, \mathbf{n}_l, \mathbf{n}'_l)$  is the oriented solid angle of the spherical triangle with vertices  $\hat{z}$ ,  $\mathbf{n}_l$ , and  $\mathbf{n}'_l$ . For the classical solitons with arbitrary spin  $S$ , the vectors  $\mathbf{n}_l$  and  $\mathbf{n}'_l$  are still *perpendicular* to the rotation  $\hat{z}$  axis, implying that we can still parametrize them with the single azimuthal angle  $\varphi_l$  because  $\theta_l = \pi/2$ . In this case, the overlap between two coherent states with  $\mathbf{n}_l$  and  $\mathbf{n}'_l$  differing by a small azimuthal shift  $\delta\varphi$  satisfies,

$$\arg(\langle \mathbf{n}_l | \mathbf{n}_l | \varphi + \delta\varphi \rangle) = S \delta\varphi \pmod{2\pi}, \tag{F2}$$

The soliton ( $\tau = +$ ) and anti-soliton ( $\tau = -$ ) states centered around the site  $j$  can then be expressed as:

$$|\varphi_{\tau}^{(j)}\rangle = \bigotimes_l |\mathbf{n}_l[\varphi_{\tau}(l-j)]\rangle, \tag{F3}$$

where  $\varphi_{\tau}(l-j)$  is the azimuthal angle of the classical soliton solution. Then, the total overlap between the soliton ( $\tau = +$ ) or anti-soliton ( $\tau = -$ ) product states,  $|\varphi_{\tau}^{(j)}\rangle$  and  $|\varphi_{\tau}^{(j+1)}\rangle$  centered at sites  $j$  and  $j+1$ , is

$$\begin{aligned}
\zeta \equiv \langle \varphi_{\tau}^{(j)} | \varphi_{\tau}^{(j+1)} \rangle &= \prod_l \langle \mathbf{n}_l[\varphi_{\tau}(l-j)] | \mathbf{n}_l[\varphi_{\tau}(l-j-1)] \rangle \\
&= |\zeta| e^{iS \Delta\Phi},
\end{aligned} \tag{F4}$$

with

$$\Delta\Phi \equiv \sum_l [\varphi_{\tau}(l-(j+1)) - \varphi_{\tau}(l-j)]. \tag{F5}$$

For a chiral soliton or anti-soliton with unit winding,  $\Delta\Phi = \pm 2\pi$  for  $\tau = \pm 1$ , we have:

$$\zeta = |\zeta| e^{\pm i 2\pi S} = |\zeta| (-1)^{2S}. \tag{F6}$$

Thus the sign of the soliton overlap alternates between integer and half-integer spin. Note that the real character of  $\zeta$  makes it independent of the  $\tau$  index:  $\zeta_+ = \zeta_-^* = \zeta_- = \zeta$ .

Consider now the DM part of  $\hat{H}_S$ ,

$$\hat{H}_{\text{DM}} = -D \sum_l \hat{h}_l, \quad \hat{h}_l = (\hat{\mathbf{S}}_l \times \hat{\mathbf{S}}_{l+1}) \cdot \hat{e}_z, \tag{F7}$$

and define,

$$h_0 = \langle \varphi_{\tau}^{(j)} | \hat{H}_{\text{DM}} | \varphi_{\tau}^{(j)} \rangle, \quad h_1 = \langle \varphi_{\tau}^{(j)} | \hat{H}_{\text{DM}} | \varphi_{\tau}^{(j+1)} \rangle. \tag{F8}$$

Using the exact identity for coherent states [62]:

$$\frac{\langle \mathbf{n}_l | \hat{S}_l^{\alpha} | \mathbf{n}'_l \rangle}{\langle \mathbf{n}_l | \mathbf{n}'_l \rangle} = S \mathcal{A}^{\alpha}(\mathbf{n}_l, \mathbf{n}'_l), \tag{F9}$$

where,

$$\mathcal{A}(\mathbf{n}_l, \mathbf{n}'_l) = \frac{\mathbf{n}_l + \mathbf{n}'_l - i \mathbf{n}_l \times \mathbf{n}'_l}{1 + \mathbf{n}_l \cdot \mathbf{n}'_l}, \quad (\text{F10})$$

one finds that,

$$\begin{aligned} h_1^\tau &= -DS^2 \sum_l (\mathcal{A}_l^\tau \times \mathcal{A}_{l+1}^\tau)_z, \\ h_0^\tau &= -DS^2 \sum_l (\mathbf{n}_l[\varphi_\tau(l-j)] \times \mathbf{n}_{l+1}[\varphi_\tau(l+1-j)])_z. \end{aligned} \quad (\text{F11})$$

with

$$\mathcal{A}_l^\tau \equiv \mathcal{A}(\mathbf{n}_l[\varphi_\tau(l-j)], \mathbf{n}_l[\varphi_\tau(l-j-1)]), \quad (\text{F12})$$

To find the sign of the nearest-neighbor soliton hopping we introduce the difference

$$\delta E_\tau \equiv \frac{\langle \varphi_\tau^{(j)} | \hat{H}_{\text{DM}} | \varphi_\tau^{(j+1)} \rangle}{\langle \varphi_\tau^{(j)} | \varphi_\tau^{(j+1)} \rangle} - \langle \varphi_\tau^{(j)} | \hat{H}_{\text{DM}} | \varphi_\tau^{(j)} \rangle. \quad (\text{F13})$$

This quantity is real because there is a symmetry transformation that exchanges the solitons centered at sites  $j$  and  $j+1$ . According to Eq. (D7), the overlaps  $\langle \varphi_\tau^{(j)} | \varphi_\tau^{(j+n)} \rangle = \mathcal{O}(\zeta^n)$  This is implies that to leading order in  $\zeta$ , the “Wannierization” of the soliton state gives:

$$\langle \Phi_\tau^{(j)} \rangle = \langle \varphi_\tau^{(j)} \rangle - \frac{\zeta}{2} \left( \langle \varphi_\tau^{(j+1)} \rangle + \langle \varphi_\tau^{(j-1)} \rangle \right) + \mathcal{O}(\zeta^2). \quad (\text{F14})$$

where the coefficients of the expansion result from imposing the orthogonality condition  $\langle \Phi_\tau^{(j)} | \Phi_\tau^{(j')} \rangle = \delta_{jj'}$ . Then, the DM-induced hopping matrix element is,

$$t_{\text{DM}}^\tau = \langle \Phi_\tau^{(j)} | \hat{H}_{\text{DM}} | \Phi_\tau^{(j+1)} \rangle = \zeta \delta E_\tau + \mathcal{O}(\zeta^2). \quad (\text{F15})$$

Hence, the sign of  $t_{\text{DM}}$  is determined by the Berry-phase factor in  $\zeta$  and the real prefactor  $\delta E_\tau$ .

Using Eq. (F6) in Eq. (F15), we obtain

$$t_{\text{DM}}^\tau = |\zeta| (-1)^{2S} \delta E_\tau, \quad (\text{F16})$$

which implies

$$\text{sgn}(t_{\text{DM}}^\tau) = \begin{cases} + \text{sgn}(\delta E_\tau), & S \text{ integer}, \\ - \text{sgn}(\delta E_\tau), & S \text{ half-integer}. \end{cases} \quad (\text{F17})$$

The remaining task is to determine the sign of  $\delta E_\tau$ . To this end, we expand to second order in

$$d_l \equiv \varphi_+(l-j-1) - \varphi_+(l-j). \quad (\text{F18})$$

The coherent-state connection expands as

$$\mathcal{A}_l^\tau = \mathbf{n}_l^{(j\tau)} + \tau \tan \frac{d_l}{2} (\hat{\mathbf{z}} \times \mathbf{n}_l^{(j)} - i \hat{\mathbf{z}}), \quad (\text{F19})$$

where we have used that  $\varphi_+ = -\varphi_-$  and  $n_l^{(j\tau)} \equiv \mathbf{n}_{l+1}[\varphi_\tau(l+1-j)]$ . This equation leads to

$$\begin{aligned} (\mathcal{A}_l^\tau \times \mathcal{A}_{l+1}^\tau)_z &= (\mathbf{n}_l^{(j\tau)} \times \mathbf{n}_{l+1}^{(j\tau)})_z - \tau \tan \frac{d_l}{2} \tan \frac{d_{l+1}}{2} \sin d_{l+1} \\ &+ \tau \left( \tan \frac{d_{l+1}}{2} - \tan \frac{d_l}{2} \right) \cos d_{l+1}. \end{aligned} \quad (\text{F20})$$

Substituting this expansion into Eq. (F13) gives

$$\begin{aligned} \delta E_\tau &= \tau DS^2 \sum_l \tan \frac{d_l}{2} \tan \frac{d_{l+1}}{2} \sin d_{l+1} \\ &- \tau DS^2 \sum_l \left( \tan \frac{d_{l+1}}{2} - \tan \frac{d_l}{2} \right) \cos d_{l+1} \end{aligned} \quad (\text{F21})$$

For smooth soliton profiles, Eq. (F18) can be Taylor expanded. In this limit, the second term is parametrically subleading: its lowest nonvanishing contribution in the gradient expansion arises only at fifth order, whereas the leading term contributes already at third order:

$$\tau \sum_l \left( \tan \frac{d_{l+1}}{2} - \tan \frac{d_l}{2} \right) \cos d_{l+1} \rightarrow \frac{a^4}{4} \int dx \partial_x \varphi_\tau (\partial_x^2 \varphi_\tau)^2.$$

Therefore, to leading order in  $d_l$ , we have

$$\delta E_\tau \simeq \tau DS^2 \sum_l \tan \frac{d_l}{2} \tan \frac{d_{l+1}}{2} \sin d_{l+1}, \quad (\text{F22})$$

which in the long wavelength (continuum) limit reduces to

$$\delta E_\tau \simeq \frac{a^2 DS^2}{4} \int dx (\partial_x \varphi_\tau(x))^3. \quad (\text{F23})$$

By using the sine-Gordon solution identity  $(\partial_x \varphi_\tau)^2 = 2m^2(1 - \cos \varphi_\tau)$ , this can be further simplified to

$$\delta E_\tau \simeq \frac{a^2 DS^2}{2} \int dx \partial_x^3 \varphi_\tau(x) - \tau a^2 \pi D^2 S^2 m^2. \quad (\text{F24})$$

We then conclude that  $\delta E < 0$  for the soliton solution ( $d_l D < 0$ ), while  $\delta E > 0$  ( $d_l D > 0$ ) for the anti-soliton solution. Because  $\delta E_\tau$  is odd under the transformation  $\tau \rightarrow -\tau$  (or equivalently,  $d_l \rightarrow -d_l$ ), the DM contribution to the hopping amplitude acquires opposite signs for soliton and anti-soliton configurations. This follows from the fact that  $\hat{H}_{\text{DM}}$  is odd under spatial inversion about site  $j$ ,  $\hat{g}_j \hat{H}_{\text{DM}} \hat{g}_j = -\hat{H}_{\text{DM}}$ , and that this inversion transforms a soliton into an antisoliton,  $\hat{g}_j | \varphi_+^{(j)} \rangle = | \varphi_-^{(j)} \rangle$ . Thus,

$$\begin{aligned} \langle \varphi_+^{(j)} | \hat{H}_{\text{DM}} | \varphi_+^{(j+1)} \rangle &= \langle \varphi_+^{(j)} | \hat{g}_j^2 \hat{H}_{\text{DM}} \hat{g}_j^2 | \varphi_+^{(j+1)} \rangle \\ &= - \langle \varphi_-^{(j)} | \hat{H}_{\text{DM}} | \varphi_-^{(j+1)} \rangle, \end{aligned} \quad (\text{F25})$$

confirming that the DM-induced hopping amplitudes for solitons and antisolitons differ by a minus sign.

Combined with Eqs. (F16) and (F17) this result yields the integer/half-integer alternation of the DM-induced soliton hopping amplitude. Solitons of the half-integer spin chain have  $t_{\text{DM}} > 0$ , while for those of the integer one  $t_{\text{DM}} < 0$ . Consequently, the Berry-phase structure enforces soliton band minima at  $k = 0$  for integer  $S$  and at  $k = \pi$  for half-integer  $S$ . The situation is reverse for anti-solitons.

Note that in this section we have evaluated only the DM contribution to the nearest-neighbor hopping amplitude. This restriction is justified because the DM term yields a contribution whose magnitude exceeds the combined contributions from the Heisenberg and Zeeman terms; consequently, the sign of  $t_1$  is fixed by the DM part computed here. That said, by following an analogous derivation, one can show that the Heisenberg and Zeeman contributions to  $t_1$  also exhibit an alternation between half-integer and integer spin, since both are linear in  $\zeta$  at leading order.

## Appendix G: Details about TEBD calculations

To compute the dynamical correlation functions, we employed the time-evolution block decimation (TEBD) method as implemented in the `ITensor.jl` (v0.9) library [36, 37]. The algorithmic steps are as follows:

1. Use DMRG to obtain the ground state  $|0\rangle$ .
2. At  $t = 0$ , apply the spin operator at site  $j'$  to the ground state:  $|\psi(0)\rangle = \hat{S}_{j'}^\beta |0\rangle$ .
3. Evolve the state in time with a small time step  $\delta t \ll 1$  using TEBD to obtain  $|\psi(t = \delta t)\rangle = e^{-i\hat{H}\delta t}|\psi(t = 0)\rangle$ .
4. Compute  $\mathcal{S}_{jj'}^{\alpha\beta}(t = \delta t) = \langle 0|S_j^\alpha|\psi(t = \delta t)\rangle$ .
5. Continue the time evolution of the initial state by repeating step 3 a total of  $n_{\text{steps}} = T_f/\delta t$  times, with  $T_f$  the total evolution time.

After completing these steps, a Fourier transformation in both space and time is applied to obtain the dynamical function. However, since the total evolution time  $T_f$  is finite ( $T_f < \infty$ ), the Fourier transform of  $\mathcal{S}_{jj'}^{\alpha\beta}(t)$  will exhibit non-physical oscillations due to the truncation in time. To avoid this effect we multiply the time-dependent correlator by a Parzen function [63],

$$W(x, a) = \begin{cases} 1 - 6\left|\frac{x}{a}\right|^2 + 6\left|\frac{x}{a}\right|^3 & \text{if } |x| \leq \frac{a}{2} \\ 2\left(1 - \left|\frac{x}{a}\right|^3\right)^3 & \text{if } \frac{a}{2} < |x| \leq a \\ 0 & \text{if } |x| > a \end{cases} \quad (\text{G1})$$

Hence, we compute,

$$\begin{aligned} \mathcal{S}_{jj'}^{\alpha\beta}(\omega) &= \int_{-T_f}^{T_f} dt e^{i\omega t} \mathcal{S}_{jj'}^{\alpha\beta}(t) W(t, T_f) \\ &= \int_{-\infty}^{\infty} dt e^{i\omega t} \mathcal{S}_{jj'}^{\alpha\beta}(t) W(t, T_f) \\ &= \frac{1}{2\pi} \int_{-\infty}^{\infty} d\omega' \mathcal{F}[\mathcal{S}_{jj'}^{\alpha\beta}(t)](\omega') \mathcal{F}[W(t, T_f)](\omega - \omega') \\ &= \frac{1}{2\pi} \mathcal{F}[\mathcal{S}_{jj'}^{\alpha\beta}(t)](\omega) * \mathcal{F}[W(t, T_f)](\omega) \end{aligned} \quad (\text{G2})$$

with the convolution kernel is:

$$\frac{1}{2\pi} \mathcal{F}[W(t, T_f)](\omega) = \frac{96 \sin^4(T_f \omega / 4)}{\pi T_f^4 \omega^4}. \quad (\text{G3})$$

The frequency resolution is determined by the standard error of the distribution which is equal to  $2\sqrt{3}/T_f$ .

Also, several symmetry properties of the correlators can be used to reduce the computational cost. Summarizing them for the case  $\alpha = \beta$  (the one relevant for us):

1.  $\mathcal{S}_{jj'}(t) = \mathcal{S}_{j'j}^*(-t)$  (Hermiticity of  $\hat{H}$ )
2.  $\mathcal{S}_{jj'}(-t) = \mathcal{S}_{jj'}^*(t)$  (Symmetry  $\mathcal{J}_R R^z(\pi)$ )
3.  $\mathcal{S}_{jj'}(t) = \mathcal{S}_{j'j}(t)$  (1 and 2)
4.  $\mathcal{S}_{jj'}(t) = \mathcal{S}(j - j', t)$  (Translational invariance)

## Appendix H: Hybridization between the single-magnon and the two-magnon bound state in the high field limit

In the high field limit  $H \geq J$ , the soliton size becomes of the order of a few lattice spacings. In this case, we can approximately think of it as a few-magnon bound state. Specifically, here we consider the two-magnon bound state and its hybridization with the single-magnon state through the DM interaction, which, as always in our paper, is directed perpendicular to the magnetic field axis. Our consideration of the magnon bound state follows closely Sec.III of the Supplementary Material of Ref.[64], which analyzed the bound magnon pair in the polarized state of the antiferromagnetic chain. This approach is easily adapted to the current case by changing the sign of the exchange  $J_1 \rightarrow -J$ . Finally, here we assume  $D \ll J$  and treat DM interaction as a perturbation that mixes one- and two-magnon subspaces.

Under these assumptions, the one-magnon state is described by the standard,

$$|k\rangle = \frac{1}{\sqrt{L}} \sum_{l=1}^L e^{ikl} \hat{S}_l^- |\uparrow\uparrow \dots\rangle = \frac{1}{\sqrt{L}} \sum_{l=1}^L e^{ikl} |l\rangle \quad (\text{H1})$$

where  $|l\rangle$  describes the state with down spin at location  $l$  and all other spins pointing up. The magnon dispersion

is given by the standard  $\epsilon_1(k) = H + J(1 - \cos(k)) = H + 2J \sin^2(k/2)$ .

The two-magnon bound state with the center of mass momentum  $K$  is given by: [64]

$$\begin{aligned} |2K\rangle &= \sum_{l,l'=1}^L \psi_{ll'} \hat{S}_l^- \hat{S}_{l'}^- |\uparrow\uparrow \dots\rangle, \\ \psi_{ll'} &= \frac{1}{2\sqrt{L}} \sin(K/2) e^{iK(l+l')/2} e^{-\gamma(|l-l'|-1)}, \\ \epsilon_2(K) &= 2H + J \sin^2(K/2), \end{aligned} \quad (\text{H2})$$

where the bound state radius  $1/\gamma$  is determined by  $K$  via  $e^{-\gamma} = \cos(K/2)$ .

Our goal is to find the overlap  $\langle 2K | \hat{H}_{\text{DM}} | k \rangle$ . Consider,

$$\begin{aligned} \hat{H}_{\text{DM}} |k\rangle &= \frac{D}{2i\sqrt{L}} \sum_{l=1}^L e^{ikl} \sum_{l'=1}^L (\hat{S}_{l'}^z - \hat{S}_{l'+2}^z)(\hat{S}_{l'+1}^+ - \hat{S}_{l'+1}^-) |l\rangle \\ &= \frac{D}{2i\sqrt{L}} \sum_{l=1}^L e^{ikl} (|l, l+1\rangle - |l-1, l\rangle), \end{aligned} \quad (\text{H3})$$

where  $|l, l'\rangle$  denotes state with down spins at  $l$  and  $l'$ . Using Eq. (H2) it is easy to find,

$$\langle 2K | \hat{H}_{\text{DM}} | k \rangle = D \sin^2(k/2) \delta_{k,K} \quad (\text{H4})$$

Clearly, the hybridization is strongest at the zone boundary,  $k = \pi$ , and is absent in the zone center,  $k = 0$ .

Therefore, the effective Hamiltonian describing the mixing of the one- and two-magnon sectors is given by the  $2 \times 2$  matrix with diagonal elements  $\epsilon_1(k)$  and  $\epsilon_2(k)$ , and the off-diagonal ones  $D \sin^2(k/2)$ . The new eigenvalues follow immediately,

$$E(k) = \frac{1}{2} \left[ \epsilon_1(k) + \epsilon_2(k) \pm \sqrt{(\epsilon_1(k) - \epsilon_2(k))^2 + 4D^2 \sin^4(k/2)} \right] \approx \begin{cases} \epsilon_2(k) + \frac{D^2}{H} \sin^4(k/2), \\ \epsilon_1(k) - \frac{D^2}{H} \sin^4(k/2). \end{cases}$$

where the last line is obtained in the  $H \gg J, D$  limit. It is also clear that DM interaction couples the 2-magnon sector to the 3-magnon one, and so on. Accounting for all of these, one should be able to reconstruct the soliton and

antisoliton excitations as multi-magnon bound states. At this stage, we refrain from the more general analysis of this interesting problem.

---

[1] J. S. Russell, Report on waves, in *Report of the 14th Meeting of the British Association for the Advancement of Science* (York, London, 1844) p. 311.

[2] J. E. Allen, The early history of solitons (solitary waves), *Physica Scripta* **57**, 436 (1998).

[3] A. D. Craik, The origins of water wave theory, *Annu. Rev. Fluid Mech.* **36**, 1 (2004).

[4] W. Hereman, Shallow water waves and solitary waves, in *Mathematics of complexity and dynamical systems* (Springer, 2012) pp. 1520–1532.

[5] N. J. Zabusky and M. D. Kruskal, Interaction of “solitons” in a collisionless plasma and the recurrence of initial states, *Physical review letters* **15**, 240 (1965).

[6] R. Rajaraman, *Solitons and Instantons: An Introduction to Solitons and Instantons in Quantum Field Theory*, North-Holland Personal Library (North-Holland, Amsterdam, 1982).

[7] J. H. Adlam and J. E. Allen, The structure of strong collision-free hydromagnetic waves, *Philosophical Magazine* **3**, 448 (1958).

[8] T. H. R. Skyrme, A non-linear field theory, *Proceedings of the Royal Society of London. Series A. Mathematical and Physical Sciences* **260**, 127 (1961).

[9] T. Skyrme, A unified field theory of mesons and baryons, *Nuclear Physics* **31**, 556 (1962).

[10] I. Zahed and G. E. Brown, The skyrme model, *Physics Reports* **142**, 1 (1986).

[11] P. Chaikin and T. Lubensky, *Principles of Condensed Matter Physics* (Cambridge University Press, 2000).

[12] A. Kosevich, B. Ivanov, and A. Kovalev, Magnetic solitons, *Physics Reports* **194**, 117 (1990).

[13] S. Coleman, Quantum sine-gordon equation as the massive thirring model, *Phys. Rev. D* **11**, 2088 (1975).

[14] S. Mandelstam, Soliton operators for the quantized sine-gordon equation, *Phys. Rev. D* **11**, 3026 (1975).

[15] I. Dzyaloshinskii, Theory of helicoidal structures in antiferromagnets. i. nonmetals, *Sov. Phys. JETP* **19**, 960 (1964).

[16] Y. A. Izyumov, Modulated, or long-periodic, magnetic structures of crystals, *Soviet Physics Uspekhi* **27**, 845 (1984).

[17] J.-i. Kishine and A. S. Ovchinnikov, Theory of monoax-

ial chiral helimagnet, in *Solid State Physics*, Solid State Physics, Vol. 66, edited by R. E. Camley and R. L. Stamps (Academic Press, 2015) pp. 1–130.

[18] A. N. Bogdanov and D. Yablonskii, Thermodynamically stable “vortices” in magnetically ordered crystals. the mixed state of magnets, *Zh. Eksp. Teor. Fiz.* **95**, 178 (1989).

[19] S. Mühlbauer, B. Binz, F. Jonietz, C. Pfleiderer, A. Rosch, A. Neubauer, R. Georgii, and P. Böni, Skyrmion lattice in a chiral magnet, *Science* **323**, 915 (2009).

[20] X. Yu, Y. Onose, N. Kanazawa, J. H. Park, J. Han, Y. Matsui, N. Nagaosa, and Y. Tokura, Real-space observation of a two-dimensional skyrmion crystal, *Nature* **465**, 901 (2010).

[21] H. Zhang, Z. Wang, D. Dahlbom, K. Barros, and C. D. Batista, Cp2 skyrmions and skyrmion crystals in realistic quantum magnets, *Nature Communications* **14**, 3626 (2023).

[22] F. Williams, D. Dahlbom, H. Zhang, S. Agarwal, K. Barros, and C. D. Batista, Skyrmions of frustrated quantum dimer systems, arXiv preprint arXiv:2506.22320 (2025).

[23] M. Nitta, Relations among topological solitons, *Phys. Rev. D* **105**, 105006 (2022).

[24] N. Manton and P. Sutcliffe, *Topological solitons* (Cambridge University Press, 2004).

[25] R. Shankar, *Quantum Field Theory and Condensed Matter: An Introduction* (Cambridge University Press, 2017).

[26] V. Zapf, M. Jaime, and C. D. Batista, Bose-einstein condensation in quantum magnets, *Rev. Mod. Phys.* **86**, 563 (2014).

[27] D. Dahlbom, H. Zhang, C. Miles, S. Quinn, A. Niraula, B. Thipe, M. Wilson, S. Matin, H. Mankad, S. Hahn, *et al.*, Sunny. jl: a julia package for spin dynamics, arXiv preprint arXiv:2501.13095 (2025).

[28] A. Luther and V. J. Emery, Backward scattering in the one-dimensional electron gas, *Phys. Rev. Lett.* **33**, 589 (1974).

[29] H.-B. Braun and D. Loss, Berry’s phase and quantum dynamics of ferromagnetic solitons, *Phys. Rev. B* **53**, 3237 (1996).

[30] S. Kodama, A. Tanaka, and Y. Kato, Spin parity effects in a monoaxial chiral ferromagnetic chain, *Phys. Rev. B* **107**, 024403 (2023).

[31] T. Giamarchi, *Quantum Physics in One Dimension*, International Series of Monographs on Physics (Clarendon Press, 2004).

[32] A. Haller, S. A. Díaz, W. Belzig, and T. L. Schmidt, Quantum magnetic skyrmion operator, *Phys. Rev. Lett.* **133**, 216702 (2024).

[33] D. Bhowmick, A. Haller, D. S. Kathyat, T. L. Schmidt, and P. Sengupta, Quantum skyrmion liquid, *Phys. Rev. B* **111**, 134410 (2025).

[34] R. Takashima, H. Ishizuka, and L. Balents, Quantum skyrmions in two-dimensional chiral magnets, *Phys. Rev. B* **94**, 134415 (2016).

[35] C. D. Batista and G. Ortiz, Generalized jordan-wigner transformations, *Phys. Rev. Lett.* **86**, 1082 (2001).

[36] M. Fishman, S. R. White, and E. M. Stoudenmire, The ITensor Software Library for Tensor Network Calculations, *SciPost Phys. Codebases* , 4 (2022).

[37] M. Fishman, S. R. White, and E. M. Stoudenmire, Codebase release 0.3 for ITensor, *SciPost Phys. Codebases* , 4 (2022).

[38] P.-O. Löwdin, On the non-orthogonality problem connected with the use of atomic wave functions in the theory of molecules and crystals, *The Journal of Chemical Physics* **18**, 365 (1950).

[39] I. Mayer, On löwdin’s method of symmetric orthogonalization, *International Journal of Quantum Chemistry* **90**, 63 (2002).

[40] M. Mekata and K. Adachi, Magnetic structure of cscocl<sub>3</sub>, *J. Phys. Soc. Jpn.* **45**, 1050–1057 (1978).

[41] A. Zheludev, S. Maslov, G. Shirane, Y. Sasago, N. Koide, and K. Uchinokura, Field-induced incommensurate-to-commensurate transition in ba<sub>2</sub>cuge<sub>2</sub>o<sub>7</sub>, *Phys. Rev. B* **57**, 2968 (1998).

[42] A. Zheludev, S. Maslov, G. Shirane, Y. Sasago, N. Koide, and K. Uchinokura, Field-induced commensurate-incommensurate phase transition in a dzyaloshinskii-moriya spiral antiferromagnet, *Phys. Rev. Lett.* **78**, 4857 (1997).

[43] K. Y. Povarov, T. A. Soldatov, R.-B. Wang, A. Zheludev, A. I. Smirnov, and O. A. Starykh, Electron spin resonance of the interacting spinon liquid, *Phys. Rev. Lett.* **128**, 187202 (2022).

[44] I. Garate and I. Affleck, Interplay between symmetric exchange anisotropy, uniform dzyaloshinskii-moriya interaction, and magnetic fields in the phase diagram of quantum magnets and superconductors, *Phys. Rev. B* **81**, 144419 (2010).

[45] Y.-H. Chan, W. Jin, H.-C. Jiang, and O. A. Starykh, Ising order in a magnetized heisenberg chain subject to a uniform dzyaloshinskii-moriya interaction, *Phys. Rev. B* **96**, 214441 (2017).

[46] Y. Shimamoto, Y. Matsushima, T. Hasegawa, Y. Kousaka, I. Proskurin, J. Kishine, A. S. Ovchinnikov, F. J. T. Goncalves, and Y. Togawa, Observation of collective resonance modes in a chiral spin soliton lattice with tunable magnon dispersion, *Phys. Rev. Lett.* **128**, 247203 (2022).

[47] O. G. Mouritsen, Specific heat of the classical easy-plane ferromagnetic chain with application to csnif<sub>3</sub>, *Physical Review B* **30**, 498 (1984).

[48] U. Balucani, A. Rettori, and V. Tognetti, Classical ferromagnetic heisenberg chain in a magnetic field, *Phys. Rev. Lett.* **48**, 703–706 (1982).

[49] J. Karadamoglou, N. Papanicolaou, X. Wang, and X. Zotos, Magnon dispersion and thermodynamics in csnif<sub>3</sub>, *Phys. Rev. B* **63**, 224406 (2001).

[50] R. Coldea, D. A. Tennant, E. M. Wheeler, E. Wawrzynska, D. Prabhakaran, M. Telling, K. Habicht, P. Smeibidl, and K. Kiefer, Quantum criticality in an ising chain: Experimental evidence for emergent e<sub>8</sub> symmetry, *Science* **327**, 177 (2010).

[51] H. Adachi, M. Ishikawa, T. Hirano, M. Ichioka, and K. Mekata, Helical magnetic structure in cscocl<sub>3</sub>, *J. Phys. Soc. Jpn.* **49**, 545–553 (1980).

[52] H. Adachi, M. Ishikawa, T. Hirano, M. Ichioka, and K. Mekata, Helical magnetic structure in cscocl<sub>3</sub>, *Journal of the Physical Society of Japan* **49**, 545 (1980).

[53] T. Nikuni and H. Shiba, Magnetic excitations in cscocl<sub>3</sub> with helical spin structure, *Journal of the Physical Society of Japan* **62**, 3268 (1993).

[54] R. Aoki, Y. Togawa, and S. Ohara, Electrical transport properties of micrometer-sized samples of the rare-earth chiral magnet ybn<sub>3</sub>al<sub>9</sub>, *Phys. Rev. B* **97**, 214414 (2018).

- [55] Y. Wang, H. Jin, J. Cao, R. Yu, J. Li, W. Tong, J. Xu, F. Zhu, Y. Wang, L. Zhang, and R. Tai, Nonequilibrium spin dynamics in the chiral soliton lattice host  $ybn_3al_9$ , *Results in Physics* **75**, 108336 (2025).
- [56] C. Psaroudaki, S. Hoffman, J. Klinovaja, and D. Loss, Quantum dynamics of skyrmions in chiral magnets, *Phys. Rev. X* **7**, 041045 (2017).
- [57] K. Mæland and A. Sudbø, Quantum fluctuations in the order parameter of quantum skyrmion crystals, *Phys. Rev. B* **105**, 224416 (2022).
- [58] A. Haller, S. Groenendijk, A. Habibi, A. Michels, and T. L. Schmidt, Quantum skyrmion lattices in heisenberg ferromagnets, *Phys. Rev. Res.* **4**, 043113 (2022).
- [59] A. P. Petrović, C. Psaroudaki, P. Fischer, M. Garst, and C. Panagopoulos, Colloquium: Quantum properties and functionalities of magnetic skyrmions, *Rev. Mod. Phys.* **97**, 031001 (2025).
- [60] S. K. Kim and O. Tchernyshyov, Mechanics of a ferromagnetic domain wall, *Journal of Physics: Condensed Matter* **35**, 134002 (2023).
- [61] H. J. Mikeska, Solitons in a one-dimensional magnet with an easy plane, *Journal of Physics C: Solid State Physics* **11**, L29 (1978).
- [62] J. M. Radcliffe, Some properties of coherent spin states, *Journal of Physics A: General Physics* **4**, 313 (1971).
- [63] Q. Li, J. Cui, and W. Li, Detecting confined and deconfined spinons in dynamical quantum simulations, *Phys. Rev. Res.* **4**, 013193 (2022).
- [64] A. Keselman, L. Balents, and O. A. Starykh, Dynamical signatures of quasiparticle interactions in quantum spin chains, *Phys. Rev. Lett.* **125**, 187201 (2020).